Dynamics of a thin film flowing down a heated wall with finite thermal diffusivity

Dallaston, MC, Tseluiko, D & Kalliadasis, S

DOI 10.1103/PhysRevFluids.1.073903
ISSN 2469-990X

Publisher: American Physical Society

Dynamics of a thin film flowing down a heated wall with finite thermal diffusivity

Michael C. Dallaston
Department of Chemical Engineering, Imperial College London, London SW7 2AZ, UK

Dmitri Tseluiko
Department of Mathematical Sciences, Loughborough University, Loughborough, LE11 3TU, UK

Serafim Kalliadasis
Department of Chemical Engineering, Imperial College London, London SW7 2AZ, UK
(Dated: October 24, 2016)

Consider the dynamics of a thin film flowing down a heated substrate. The substrate heating generates a temperature distribution on the free surface which in turn induces surface-tension gradients and corresponding thermocapillary stresses that affect the free surface and therefore the fluid flow. We study here the effect of finite substrate thermal diffusivity on the film dynamics. Linear stability analysis of the full Navier–Stokes and heat transport equations indicates that if the substrate diffusivity is sufficiently small, the film becomes unstable at a finite wavelength and at a Reynolds number smaller than that predicted in the long-wavelength limit. This property is captured in a reduced-order system of equations derived using a weighted-residual integral-boundary-layer method. This reduced-order model is also used to compute the bifurcation diagrams of solution branches connecting the trivial flat film to traveling waves including solitary pulses. The effect of finite diffusivity is to separate a simultaneous Hopf/transcritical bifurcation into its individual component bifurcations. The appropriate Hopf bifurcation then connects only to the solution branch of negative-hump pulses, with wave speed less than the linear wave speed while the branch of positive-single-hump pulses merges with the branch of positive-two-hump pulses at a supercritical Reynolds number. In the regime where finite-wavelength instability occurs, there exists a Hopf-bifurcation pair connected by a branch of periodic solutions, whose period cannot be increased indefinitely. Numerical simulation of the reduced-order system shows the development of a train of coherent structures each of which resembles a stationary positive-hump pulse, and, in the regime of finite-wavelength instability, wavelength selection and saturation to periodic traveling waves.

I. INTRODUCTION

Since the seminal work of Kapitza and Kapitza [1], there has been great interest in the stability of thin films flowing down inclined or vertical substrates. In the absence of any additional complexities such as thermocapillary effects, a falling film is hydrodynamically unstable for a Reynolds number (defined as the ratio of an average flow rate over the fluid's kinematic viscosity) above a critical value, which vanishes for the vertical case. In fact, one can distinguish between surface-mode and shear-mode instabilities [2]. With the exception of very slight inclines (on the order of half a degree), the critical Reynolds number at which the surface mode becomes unstable is significantly less than that for the shear mode, so at moderate Reynolds number the surface mode is the dominant one. This mode is referred to as the H-mode of instability [3, 4].

Uniformly heating the fluid from below introduces further instability due to the thermocapillary Marangoni effect. The linear-stability characteristics of falling films in this case were studied in [3, 5]. Again, there are two modes of instability. A sufficiently thick film can develop Marangoni–Bénard convections cells [6]. This instability exists even in the absence of interfacial deformation. For thinner films, the dominant mode of instability is instead due to the temperature gradient that forms along the free surface when it is deformed, given a cross-stream temperature gradient. These instability modes are referred to as the P- and S-modes [3, 4] and they both interact non-trivially with the hydrodynamic instabilities. Here, we consider parameter regimes where the H- and S-mode instabilities are most important. Each of these instabilities is a long-wave variety, in that the unstable band of wavenumbers extends to zero for a given supercritical Reynolds number; following the classification by Cross and Hohenberg [7], such dispersion curves are of type II.

There has been considerable research in the modeling of falling films in the presence of thermocapillary Marangoni effects induced by uniform [8–13] or localized heating [14–16], and even chemical reactions where the reaction rate is taken to be temperature-dependent so that heat is released into or absorbed from the film [17–19]. Such heat generation or loss gives rise to thermocapillary stresses at the interface, which, in turn, affect the dynamics of the interface. The coupling between thermocapillary Marangoni effects and substrate topography has also been analyzed [20, 21].

To avoid dealing with full systems of equations governing thin-film flows, various low-dimensional models that are better suited for both numerical and analytical treatment have been derived. The cornerstone of all low-dimensional models for thin-film flows is the so-called long-wave approximation (or lubrication approximation for vanishing Reynolds number) in which the interface slope is small and varies slowly with time, appropriate for slow flows with strong surface tension effects. The corresponding small parameter is the ratio of an average film thickness over a long lengthscale, the so-called film parameter, measuring the variation of the interface in the streamwise direction. For a falling film in the absence of any additional complexities, a naive expansion in this parameter up to first-order (including the surface tension at leading order) leads to the Benney equation [22, 23] for the film thickness, which has the same linear stability characteristics as the Navier–Stokes (NS) equations in the long-wave limit, and is accurate in the nonlinear regime for near-critical Reynolds numbers [4, 24]. However, for even moderate supercritical Reynolds numbers, the solution branch of single-hump solitary pulses of the Benney equation exhibits turning points and non-existence of single-hump solitary-pulse solutions, whereas experimental studies and direct numerical simulations of the NS equations for these Reynolds numbers show that the evolution of the film is characterized by a train of coherent structures each of which resembles single-hump solitary pulse [4]. Also, when the Benney equation is integrated numerically in the region where solitary waves do not exist, it blows up in finite time, a clearly unrealistic behavior [25–27]. Thus, the Benney equation is ill-suited for modeling supercritical flows.

A way out is to introduce additional degrees of freedom. By assuming that the velocity profile is approximately parabolic even deeply in the nonlinear regime, and integrating the boundary-layer equations over the film thickness, Shkadov [28] derived a coupled system of equations for the film height and flow rate, in a manner analogous to the von Kármán–Pohlhausen method used in boundary-layer theory in aerodynamics, e.g., [29, 30]. This approach avoids the finite-time blow-up of the Benney equation but does not exhibit the correct linear stability characteristics, as far as neutral and critical conditions are concerned, except for large inclination angles [4, 24]. A modification of this approach, introduced by Ruyer-Quil and Manneville [4, 24, 31, 32], referred to at times as the weighted-residual integral-boundary-layer (WRIBL) method, corrects these drawbacks by weighting the integrals of the boundary-layer equations by the assumed form of the velocity profile, akin to a low-order Galerkin method. The WRIBL method may be extended to higher powers of the film parameter, resulting in a larger number of time- and space-dependent variables, although the governing PDEs for these variables quickly become unmanageable. A convenient compromise is the simplified second-order model put forward by Ruyer-Quil and Manneville [31, 32], which contains terms up-to-and-including second order in the film parameter, and thus includes the second-order viscous dispersion effects, but has only two independent variables like the Shkadov model. The simplified second-order model is particularly important when studying the interaction between solitary pulses. Indeed, viscous dispersion strongly influences the amplitude and frequency of the capillary ripples preceding solitary pulses, which in turn can have some crucial consequences on the nonlinear dynamics of the film and the wave-selection process in the spatiotemporal evolution [33]. After all,

solitary pulses interact through their tails which overlap.

For heated substrates, a full continuum description of the film consists of the NS equations for the fluid flow, coupled with the energy equation for the fluid that contains the combined effect of heat convection and diffusion, and subjected to appropriate wall and free-surface boundary conditions. The energy equation for the fluid can also be included in a WRIBL framework, e.g., [9–13, 15, 16].

However, the majority of previous studies involving thermocapillary effects induced by wall heating have ignored heat transport within the wall itself, thus bypassing the more involved conjugate heat transport problem. There are some exceptions, as follows. [34, 35] study linear stability properties and nonlinear evolution of a thin film flowing down an inclined heated wall and take into account the thermal conductivity and thickness of the wall. These studies are performed entirely within the context of a Benney-type equation, which has severe limitations as noted above. In this approximation, the temperature profile in both the film and the substrate is slaved to the local film thickness, and the effect of transient heat flow in the wall as the local film height changes is neglected. For this to be justified, the timescales of cross-stream thermal diffusion both in the liquid and in the substrate must be assumed to be small enough. Since the timescale of cross-stream thermal diffusion in the substrate is inversely proportional to the thermal diffusivity of the substrate, we say the corresponding Benney-type equation is valid for *large* substrate diffusivity.

The effect of non-uniform thermal conductivity of an horizontal substrate on thin-film dynamics is considered in [36] where the hydrodynamics is modeled using the lubrication approximation (where inertia is neglected). The films considered are, therefore, always hydrodynamically stable; the issue of finite-time blow-up of Benney-type equations is thus avoided, but the equation cannot be used to analyze the effects of the conjugate heat transfer on the development of solitary pulses, which only exist for supercritical Reynolds numbers. Similarly to [34, 35], the timescales of cross-stream thermal diffusion in the liquid and the substrate are taken to be small enough so that the temperature profile in the film and the substrate is slaved to the local film thickness. In [37], this study is extended to include the regime in which the timescale of cross-stream thermal diffusion within the substrate can no longer be neglected, so that the temperature profile is not determined (to leading order) by the film thickness. We refer to this as *finite* (rather than *large*) substrate diffusivity. In that paper, the dominant heat loss at the liquid-air interface is assumed to be due to evaporation, which results in a simple, constant heat flux condition at the substrate-liquid boundary not dependent on the film thickness. This allows the full heat equation for the wall temperature to be solved semi-analytically using separation of variables or a Laplace transform method. Again, the thin film is modeled using the lubrication approximation assuming a horizontal substrate, so the study does not consider parameter regimes in which solitary pulses occur.

Other studies that have considered heat flow within the substrate are [38], which examines the combined effects of conjugate heat transfer and topography both experimentally and numerically by solving the full system of governing equations (in a low-Reynolds-number regime), and [39], which focuses on the importance of substrate heat conduction near the contact line of an evaporating droplet.

In this study, we develop and analyze a WRIBL model of coupled fluid and wall heat flow including finite diffusivity of the substrate, derived from the NS/energy equations for both the fluid and the wall and appropriate wall and free-surface boundary conditions. Our aim is to use this model to examine the quantitative and qualitative effect that finite substrate diffusivity has on the stability and dynamics of the film, including the properties of solitary pulses. We thus explore a regime not modeled by either [34, 35], which do not consider the effect of finite substrate diffusivity and do not use the more widely applicable weighted-residual model, or [36, 37], which only model low-Reynolds-number flows. In order to isolate the effect of finite substrate diffusivity, we assume large thermal diffusivity in the liquid film. We demonstrate that the linear stability characteristics of our WRIBL model are in good agreement with the Orr–Sommerfeld (OS) analysis of the full NS/energy equations and associated boundary conditions. We also construct detailed bifurcation diagrams for traveling-wave solutions of our WRIBL model. Finally, we perform time-dependent computations of the model. We show that the long-time evolution is a train of soliton-like coherent structures for both the free surface and the wall temperature which interact indefinitely with each other and which resemble the infinite-domain solitary pulses.

In Sec. II, we give the governing equations, namely, NS equations in the fluid, and energy equations in both the fluid and the substrate, along with associated wall and free-surface boundary conditions. In Sec. III, we examine the linear stability characteristics of the full model using OS analysis; the most notable effect of finite substrate diffusivity is the existence of parameter values for which the onset of instability occurs at a finite wavelength, rather than at infinite wavelength as is the case for large diffusivity. In Sec. IV, we derive a WRIBL model that includes the transient effect of heat conduction in the solid substrate, which also captures the finite-wavelength instability predicted by OS, and compute the parameter regimes in which this instability is possible. In Sec. V, we explore the bifurcation structure of traveling-wave solutions to the WRIBL model from the flat film, and use numerical continuation to compute solitary pulses by increasing the period of the traveling waves. In Sec. VI, we address the question of relevance of these solutions in time-dependent computations, which, in turn, is related to the way they attract initial conditions. Finally, a discussion of our results and possible future directions is offered in Sec. VII.

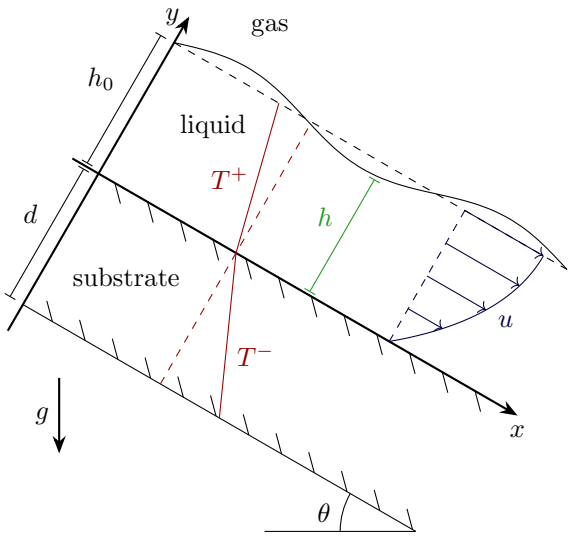

FIG. 1: Sketch of the profile geometry for a liquid film flowing down a heated wall of finite thickness d inclined at an angle θ with respect to the horizontal. h_0 is a typical film thickness and $h(x,t)$ is the local film thickness with respect to a Cartesian coordinate system (x,y) with the origin on the upper side of the wall, with x being the streamwise coordinate and y being the outward-pointing coordinate normal to the wall. Heat from the constant-temperature bottom of the plate is conducted through the solid and liquid as well as being advected in the liquid layer. The heating induces a temperature gradient on the free surface which in turn causes thermocapillary Marangoni stresses there. The parabolic profile of velocity u and piecewise linear profiles of temperature T^- and T^+ in the substrate and liquid, respectively, for the steady unidirectional flow are also shown.

II. FORMULATION

A. Problem definition, governing equations and scalings

Consider a Newtonian liquid film of characteristic thickness h_0 flowing down a flat substrate of constant thickness d, inclined at an angle θ from the horizontal, as illustrated in Fig. 1. The acceleration due to gravity is g. The fluid has kinematic viscosity ν, density ρ, thermal conductivity κ and thermal diffusivity α defined as $\alpha = \kappa/\rho c_P$, where c_P is the constant-pressure heat capacity of the liquid. The solid substrate has thermal conductivity and diffusivity α_s and κ_s, respectively. The lower boundary of the wall is taken to be at constant temperature T_b, while above the liquid, the ambient temperature and pressure are T_a and p_a, respectively.

We assume that the flow is two-dimensional and introduce a Cartesian coordinate system (x,y) with the x-axis pointing along the substrate-liquid interface in the direction of the liquid flow and the y-axis pointing outward of the substrate. The free surface of the film is defined by $y = h(x,t)$, where t is time. We now non-dimensionalize each of the variables as follows:

$$\begin{aligned} &x \mapsto lx, \quad y \mapsto \begin{cases} dy^- & \text{in the substrate} \\ h_0 y^+ & \text{in the film} \end{cases}, \quad h \mapsto h_0 h, \quad u \mapsto \frac{h_0^2 g \sin\theta}{2\nu} u, \\ &v \mapsto \frac{h_0^3 g \sin\theta}{2l\nu} v, \quad t \mapsto \frac{2l\nu}{h_0^2 g \sin\theta} t, \quad p \mapsto p_a + (\rho h_0 g \sin\theta) p, \quad T^\pm \mapsto T_a + (T_b - T_a) T^\pm. \end{aligned} \tag{1}$$

Here, l denotes a characteristic length scale in the streamwise direction and the Nusselt scaling (e.g., [10]) has been utilized for the fluid flow; u, v denote the streamwise and cross-stream velocity components, respectively, p is the liquid pressure and T^+, T^- are the temperatures in the liquid film and in the substrate, respectively.

The dimensionless NS equations for the fluid (in $0 < y^+ < h$) are

$$u_x + v_{y^+} = 0, \tag{2a}$$

$$\epsilon \mathrm{Re}(u_t + u u_x + u v_{y^+}) = -2\epsilon p_x + \epsilon^2 u_{xx} + u_{y^+y^+} + 2, \tag{2b}$$

$$\epsilon^2 \mathrm{Re}(v_t + u v_x + v v_{y^+}) = -2 p_{y^+} + \epsilon^3 v_{xx} + \epsilon v_{y^+y^+} - 2\mathrm{Ct}, \tag{2c}$$

where we have introduced the film or gradient parameter, ϵ, the Reynolds number, Re, and the inclination number, Ct:

$$\epsilon = \frac{h_0}{l}, \qquad \mathrm{Re} = \frac{h_0^3 g \sin\theta}{2\nu^2}, \qquad \mathrm{Ct} = \cot\theta. \tag{3}$$

As far as heat transport is concerned, we need the energy equation for the two phases: solid and liquid where heat is being transported via conduction and conduction and convection, respectively. We also assume that heating by viscous dissipation is negligible compared to the prescribed heat at the lower boundary, and that the specific heat is constant. The equations governing the temperature in the film and substrate are

$$\epsilon \,\mathrm{Pr}\,\mathrm{Re}(T^+_t + uT^+_x + vT^+_{y^+}) = \epsilon^2 T^+_{xx} + T^+_{y^+y^+}, \qquad 0 < y^+ < h, \tag{4a}$$

$$\epsilon A T^-_t = \epsilon^2 D^2 T^-_{xx} + T^-_{y^-y^-}, \qquad -1 < y^- < 0, \tag{4b}$$

respectively, where we have introduced the Prandtl number, Pr, the substrate-film thickness ratio, D, and a dimensionless parameter A inversely proportional to the thermal diffusivity of the substrate:

$$\mathrm{Pr} = \frac{\nu}{\alpha}, \qquad D = \frac{d}{h_0}, \qquad A = \frac{d^2 h_0 g \sin\theta}{2\alpha_s \nu}. \tag{5}$$

Physically, the group ϵA may be considered as the ratio of timescales of cross-stream heat diffusion in the solid to streamwise convection in the fluid. This group is thus a kind of Péclet number, although it compares advection and diffusion in different regions and directions. It is the neglect or inclusion of the term on the left hand side of (4b) that distinguishes between large or finite substrate diffusivity, respectively, as described in the Introduction. Note that we take the substrate-film thickness ratio D to be order one. If the substrate is much thicker than the film ($D \gg 1$) then the streamwise heat diffusion term in (4b) also becomes non-negligible; we do not consider that problem in the present study.

To close our system of equations, we require boundary conditions for the liquid film, as well as for the flow of heat. To model the effect of thermocapillary Marangoni stress on the free boundary of the film, we assume a linear constitutive relation for the surface tension σ. In dimensional variables, this relation takes the form $\sigma = \sigma_0 - \gamma(T^+ - T_a)$, where σ_0 is the surface tension at the ambient temperature T_a, and $\gamma > 0$ for most fluids, as increased temperature decreases surface tension. Under the above non-dimensionalization, the no-slip/no-penetration conditions, the kinematic condition and the normal and tangential stress balances are

$$u = 0, \qquad y^+ = 0, \tag{6a}$$

$$v = 0, \qquad y^+ = 0, \tag{6b}$$

$$h_t = v - uh_x, \qquad y^+ = h, \tag{6c}$$

$$-p - \frac{\epsilon u_x(1-\epsilon^2 h_x^2)}{1+\epsilon^2 h_x^2} - \frac{\epsilon(u_{y^+} + \epsilon^2 v_x)h_x}{1+\epsilon^2 h_x^2} = \frac{\epsilon^2(\mathrm{We} - \mathrm{Ma}\,T^+)h_{xx}}{(1+\epsilon^2 h_x^2)^{3/2}}, \qquad y^+ = h, \tag{6d}$$

$$(u_{y^+} + \epsilon^2 v_x)\frac{1-\epsilon^2 h_x^2}{1+\epsilon^2 h_x^2} - \frac{4\epsilon^2 u_x h_x}{1+\epsilon^2 h_x^2} = \frac{-2\epsilon \mathrm{Ma}(T^+_x + h_x T^+_{y^+})}{\sqrt{1+\epsilon^2 h_x^2}}, \qquad y^+ = h, \tag{6e}$$

where the dimensionless parameters We and Ma are the Weber and the Marangoni numbers, respectively, defined as

$$\mathrm{We} = \frac{\sigma_0}{\rho h_0^2 g \sin\theta}, \qquad \mathrm{Ma} = \frac{\gamma(T_b - T_a)}{\rho h_0^2 g \sin\theta}. \tag{7}$$

Finally, appropriate boundary conditions for the temperature are a prescribed condition on the lower boundary of the substrate, continuity of temperature and heat flux at the substrate-liquid interface, and Newton's law of cooling at the liquid-air interface. The non-dimensional boundary conditions for T^+ and T^- are, therefore,

$$T^- = -1, \qquad y^- = -1, \tag{8a}$$

$$T^+ = T^-, \qquad y^+ = y^- = 0, \tag{8b}$$

$$KT^+_{y^+} = T^-_{y^-}, \qquad y^+ = y^- = 0, \tag{8c}$$

$$\frac{T^+_{y^+} - \epsilon^2 h_x T^+_x}{\sqrt{1+\epsilon^2 h_x^2}} = -\mathrm{Bi}\,T^+, \qquad y^+ = h. \tag{8d}$$

The non-dimensional parameters introduced here are the liquid-air Biot number Bi and the substrate-liquid Biot number K, which contains the conductivity ratio of the liquid over the substrate,

$$\mathrm{Bi} = \frac{\beta h_0}{\kappa_l}, \qquad K = \frac{\kappa_l d}{\kappa_s h_0}, \tag{9}$$

where β is the heat-transfer coefficient describing the rate of heat transport from the liquid to the ambient gas phase.

The gradient parameter ϵ can be eliminated from the equations by rescaling $x \mapsto \epsilon x$ and $t \mapsto \epsilon t$. We assume this additional rescaling for the remainder of our study. Note that the system of equations that is obtained after such a rescaling is the same as Eqs. (2), (4), (6), (8) with ϵ set to unity. This is a formal "simplification" and does not imply we are not in the thin-film regime; rather, the order of each term in the governing equations and associated wall and free-surface boundary conditions in ϵ becomes implicit.

Given the large number of parameters involved in our model, a complete investigation over the entire parameter space would be very cumbersome. Hence, in the analysis that follows we fix the inclination angle θ, the Prandtl number Pr, the substrate-film thickness ratio D, the Weber number We and the Marangoni number Ma, and we focus on the effect of changing the Reynolds number Re, the liquid-air and the substrate-liquid Biot numbers Bi and K, and parameter A measuring the importance of substrate diffusivity. As far as A is concerned, $O(1)$ values of this parameter correspond to large substrate diffusivity, so that the temperature in the substrate may be taken to be quasi-steady. For $A = O(\epsilon^{-1})$, transient behavior of the heat in the substrate occurs on the same timescale as the evolution of the film thickness h, and can no longer be neglected; this regime is the main focus of our study.

III. LINEAR STABILITY ANALYSIS

We now examine the linear stability characteristics of the base state consisting of the unidirectional flow with a semi-parabolic velocity profile and the piecewise linear temperature profile. For this purpose, we will perform a linearization of the NS and heat transport equations (2), (4), and the associated boundary conditions (6), (8), around the base state to obtain the corresponding OS problem. This analysis is a generalization of the constant-wall temperature analysis first performed in [3].

The Nusselt flat-film solution to (2), (4), (6), (8), is (recall ϵ has been eliminated from the equations by rescaling x and t)

$$\begin{gathered} u_0 = y^+(2-y^+), \quad v_0 = 0, \quad h_0 = 1, \quad p_0 = \mathrm{Ct}(h-y^+), \\ T_0^- = \frac{1+\mathrm{Bi}-\mathrm{Bi}Ky^-}{1+\mathrm{Bi}+\mathrm{Bi}K}, \quad T_0^+ = \frac{1+\mathrm{Bi}-\mathrm{Bi}y^+}{1+\mathrm{Bi}+\mathrm{Bi}K}. \end{gathered} \tag{10}$$

We now consider the stability of this solution to infinitesimal perturbations in the form of normal modes, $u \sim u_0 + u_1(y^+)\exp(\mathrm{i}k(x-ct))$, and similarly for the other variables, where k is the wavenumber and c is the (complex) phase speed. The governing equations (2), (4) yield,

$$\mathrm{i}ku_1 + v_1' = 0, \qquad 0 < y^+ < 1, \tag{11a}$$

$$\mathrm{Re}(-\mathrm{i}cku_1 + \mathrm{i}ku_0u_1 + u_0'v_1) = -2\mathrm{i}kp_1 - k^2u_1 + u_1'', \qquad 0 < y^+ < 1, \tag{11b}$$

$$\mathrm{Re}(-\mathrm{i}ckv_1 + u_0\mathrm{i}kv_1) = -2p_1' - k^2v_1 + v_1'', \qquad 0 < y^+ < 1, \tag{11c}$$

$$\mathrm{Re}\,\mathrm{Pr}(-\mathrm{i}ckT_1^+ + u_0\mathrm{i}kT_1^+ + T_0^{+\prime}v_1) = -k^2T_1^+ + T_1^{+\prime\prime}, \qquad 0 < y^+ < 1, \tag{11d}$$

$$-\mathrm{i}AckT_1^- = -D^2k^2T_1^- + T_1^{-\prime\prime}, \qquad -1 < y^- < 0, \tag{11e}$$

where primes indicate derivatives with respect to y^+ or y^-, as appropriate. The linearization of the boundary conditions (6), (8) gives

$$u_1 = 0, \qquad y^+ = 0, \tag{11f}$$

$$v_1 = 0, \qquad y^+ = 0, \tag{11g}$$

$$-\mathrm{i}ckh_1 = v_1 - u_0\mathrm{i}kh_1, \qquad y^+ = 1, \tag{11h}$$

$$p_1 + p_0'h_1 = (\mathrm{We} - \mathrm{Ma}T_0^+)k^2h_1 + v_1', \qquad y^+ = 1, \tag{11i}$$

$$u_1' + u_0''h_1 + \mathrm{i}kv_1 = -2\mathrm{Ma}(\mathrm{i}kT_1^+ + \mathrm{i}kT_0^{+\prime}h_1), \qquad y^+ = 1, \tag{11j}$$

$$T_1^- = 0, \qquad y^- = -1, \tag{11k}$$

$$T_1^- = T_1^+, \qquad y^+ = y^- = 0, \tag{11l}$$

$$T_1^{+\prime} = -\mathrm{Bi}(T_1^+ + T_0^{+\prime}h_1), \qquad y^+ = 1. \tag{11m}$$

To reduce the number of variables, we introduce the stream-function correction ψ_1, where $u_1 = \psi_1'$ and $v_1 = -\mathrm{i}k\psi_1$, which when substituted in (11b), (11c) and (11e), and eliminating pressure p_1 between (11b) and (11c), results in the governing equations for ψ_1 and T_1^+:

$$-\mathrm{i}k\mathrm{Re}(c-u_0)(\psi_1''-k^2\psi_1)+2\mathrm{i}k\mathrm{Re}\psi_1=\psi_1''''-2k^2\psi_1''+k^4\psi_1, \tag{12a}$$

$$-\mathrm{i}k\mathrm{Re}\,\mathrm{Pr}(c-u_0)T_1^+-\mathrm{Re}\,\mathrm{Pr}\;\mathrm{i}kT_0^{+\prime}\psi_1=T_1^{+\prime\prime}-k^2T_1^+. \tag{12b}$$

Two boundary conditions for ψ_1 come from the no-slip/no-penetration conditions on the wall while the other two come from the stress conditions. Using (11b) to eliminate p_1 from the normal stress balance condition (11i), and the kinematic condition (11h) to eliminate h_1, the boundary conditions for ψ_1 are

$$\psi_1=\psi_1'=0, \qquad y^+=0, \tag{12c}$$

$$\psi_1'''-3k^2\psi_1'+\mathrm{i}k\mathrm{Re}(c-1)\psi_1'=2\mathrm{i}k\left[\frac{\mathrm{Ct}+k^2(\mathrm{We}-\mathrm{Ma}T_0^+)}{c-1}\right]\psi_1, \qquad y^+=1, \tag{12d}$$

$$\psi_1''-\frac{2\psi_1}{c-1}+k^2\psi_1=-2\mathrm{i}k\mathrm{Ma}\left(T_1^++\frac{T_0^{+\prime}\psi_1}{c-1}\right), \qquad y^+=1. \tag{12e}$$

The temperature in the solid can be solved in terms of the unknown wall temperature perturbation amplitude $T_1^+(0)$:

$$T_1^-=T_1^+(0)\frac{\sinh\left(\sqrt{D^2k^2-Aick}(y^-+1)\right)}{\sinh\sqrt{D^2k^2-Aick}}.$$

This provides a Robin condition for T^+ at $y^+=0$ as well as on the free surface:

$$KT_1^{+\prime}=\frac{\sqrt{D^2k^2-Aick}}{\tanh\sqrt{D^2k^2-Aick}}T_1^+, \qquad y^+=0, \tag{12f}$$

$$T_1^{+\prime}=-\mathrm{Bi}\left(T_1^++\frac{T_0^{+\prime}\psi_1}{c-1}\right), \qquad y^+=1. \tag{12g}$$

For given k, the OS linear system (12) has a countably infinite number of complex eigenvalues, $c=c(k)$. The stability of the flat film is determined by the sign of the largest growth rate $\sigma=\Im(kc)$, where $\Im(\cdot)$ indicates imaginary part. Noting that $z/\tanh z\to 1$ as $z\to 0$, the linear problem has trivial solution when $k=0$, corresponding to a change in the leading-order film thickness:

$$\psi_{10}=Cy^{+2}, \qquad T_{10}^+=\frac{C\mathrm{Bi}^2(y^++K)}{(1+\mathrm{Bi}+\mathrm{Bi}K)^2}. \tag{13}$$

Here, C is an arbitrary constant. This solution is the leading-order term in the small-k expansion that we describe in the next subsection, and also serves a starting point for the numerical computation of the OS problem (12). We solve the linear system (12) numerically, using the open-source numerical continuation package AUTO07p [40], in a manner similar to that described in [4]. Results are depicted in Fig. 2 for $A=0,10,100$, and representative values $\mathrm{We}=100$, $\mathrm{Ma}=15$, $\mathrm{Ct}=\cot(\pi/12)\approx 3.7$, $\mathrm{Bi}=1$, $K=1$, and $D=1$.

Figure 2(a) depicts the neutral curve $\mathrm{Re}=\mathrm{Re}^*(k)$, defined by the value of the Reynolds number such that $\sigma=0$, thus dividing the (k,Re)-plane into regions in which the flat film is stable ($\mathrm{Re}<\mathrm{Re}^*$) and unstable ($\mathrm{Re}>\mathrm{Re}^*$) to a perturbation of wavenumber k. Although it does not change the long-wave limiting value $\mathrm{Re}^*(0)$, the effect of finite substrate diffusivity is to lower the neutral curve, for $k>0$, and thus increase the range of unstable wavenumbers.

The minimum Re_c of Re^* is the critical Reynolds number, the value at which the film first becomes unstable. For small A, this minimum occurs at $k=0$ and $\mathrm{Re}=\mathrm{Re}^*(0)=\mathrm{Re}_0$ [see (15) below], which corresponds to the long-wavelength limit. If A is sufficiently large, however, the neutral curve is non-monotonic in k. When this non-monotonicity occurs, the critical Reynolds number satisfies $\mathrm{Re}_c<\mathrm{Re}_0$ and corresponds to a non-zero k, thus the type of instability changes from a long-wavelength variety to a finite-wavelength one. Figure 2(b) depicts the growth rate σ for $A=100$ and a Reynolds number $\mathrm{Re}=0.77$ that satisfies $\mathrm{Re}_c<\mathrm{Re}<\mathrm{Re}_0$. In this regime, there is a band of unstable wavenumbers which does not extend to $k=0$; in the language of Cross and Hohenberg [7], the instability has changed from type II to type I and is reminiscent of Turing-type dispersion curves (e.g., [41]) with a band of unstable wavenumbers away from zero wavenumber but with a neutral mode always at zero wavenumber. In this regime, we also see selection of a preferred wavelength like in the regime with type II dispersion curve. But unlike the regime with a type II curve where we find stationary (in a moving frame) solitary wave solutions, in the regime associated with a type I curve we find stationary periodic waves which cannot tend to the solitary-wave limit (details are given in in Sec. V).

A. Small-k behavior of the neutral curve

From the numerical results depicted in Fig. 2, it is clear that there are parameter values for which the neutral curve is not monotonic in k, implying that the flat film becomes linearly unstable to a finite wavelength perturbation at a critical Reynolds number less than the value Re_0 at $k = 0$. In principle, this behavior can be deduced analytically by expanding the OS equations in powers of k, taking

$$\begin{aligned} \psi_1 &\sim \psi_{10} + k\psi_{11} + k^2\psi_{12} + k^3\psi_{13} + \cdots, \\ T_1^+ &\sim T_{10}^+ + kT_{11}^+ + k^2T_{12}^+ + k^3T_{13}^+ + \cdots, \end{aligned} \tag{14}$$

and $c \sim c_0 + k^2c_2 + \cdots$, $\mathrm{Re}^* \sim \mathrm{Re}_0 + k^2\mathrm{Re}_2 + \cdots$; the neutral curve $\mathrm{Re} = \mathrm{Re}^*$ is set by taking the odd terms of c (which are imaginary) to be zero. To find the first correction term, it is necessary to go to third order in k, with the $O(1)$ and $O(k)$ terms giving c_0 and Re_0, and $O(k^2)$ and $O(k^3)$ terms giving c_2 and Re_2, respectively.

In practice, this process involves unwieldy polynomial solutions for ψ_1 and T_1^+, as each order in k involves integrating four times for ψ_1, and twice for T_1^+. The expansion is readily found using a computer algebra system such as Maple, but the resulting formula for Re_2 is too complicated to report, chiefly due to terms involving the Prandtl number Pr (arising from convection of heat in the fluid). However, these terms may formally be neglected on the assumption that $\mathrm{Pr} = O(1)$, while $\mathrm{We} = O(\epsilon^{-2})$ and $A = O(\epsilon^{-1})$. As we are interested in the competing effects of surface tension and finite diffusivity in the substrate, we include only the dominant terms proportional to We and A^2 in Re_2:

$$\mathrm{Re}^* \sim \mathrm{Re}_0 + k^2\mathrm{Re}_2, \tag{15a}$$

where

$$\mathrm{Re}_0 = \frac{5}{4}\mathrm{Ct} - \frac{15}{8}\frac{\mathrm{MaBi}}{(1+\mathrm{Bi}+\mathrm{Bi}K)^2}, \tag{15b}$$

$$\mathrm{Re}_2 = \frac{5}{4}\mathrm{We} - \frac{6+6\mathrm{Bi}+\mathrm{Bi}K}{6(1+\mathrm{Bi}+\mathrm{Bi}K)^4}A^2\mathrm{Bi}^2\mathrm{Ma}K + \mathrm{h.o.t.}, \tag{15c}$$

where the higher-order terms (h.o.t.) of $O(\epsilon^{-1})$ and above have been neglected in Re_2. The long-wave limit Re_0 at $k = 0$ is identical to that obtained for a finite-thickness wall with infinite thermal diffusivity $A = 0$ found using the long-wave approximation in [34].

The second term Re_2 allows us to estimate the effect of A on the behavior of Re^* near $k = 0$. While we expect surface tension to stabilize sufficiently short wavelengths (so that $\mathrm{Re}^* \to \infty$ as $k \to \infty$, as the numerical results depict), if $\mathrm{Re}_2 < 0$, then Re^* is decreasing close to $k = 0$, and we thus observe the non-monotonic behavior seen in the numerical solution of the OS problem (12), that results in short-wave instability for $\mathrm{Re}_c < \mathrm{Re} < \mathrm{Re}_0$.

IV. WEIGHTED-RESIDUAL APPROACH

A. Formulation

Given the shortcomings of the Benney equation discussed in the Introduction, we use a weighted-residual approach to obtain a first-order WRIBL model. Details of this method are found in numerous sources, e.g., [4, 10–13, 31, 32]. Since surface tension is considered to be important at leading order, we formally assume $\mathrm{We} = O(\epsilon^{-2})$ as already done in the previous section, while other dimensionless parameters relating to the fluid flow (Re, Ct, Ma) are taken to be $O(1)$.

The velocity profile u is assumed to be parabolic in y^+ and dependent on both the film thickness h and the flow rate (per unit length in the transverse direction) $q(x,t)$, both of which are are unknown functions of x and t:

$$u = \frac{3q}{h^3}\left(hy^+ - \frac{1}{2}y^{+2}\right) + \frac{\mathrm{Ma}\tau_x}{h}\left(hy^+ - \frac{3}{2}y^{+2}\right), \tag{16}$$

where $\tau(x,t) = T^+(x,h(x,t),t)$ is the surface temperature. The coefficients in (16) are chosen to be compatible with the no-slip condition (6a), the tangential stress balance (6e) and the integral relationship between the velocity and the flow rate, $q = \int_0^h u\,\mathrm{d}y^+$. The assumed form (16) for u is then substituted into the x-component of the momentum equation (2b), whereby pressure p is eliminated using the y-component of the momentum equation and the normal stress balance, and vertical velocity v is eliminated using conservation of mass.

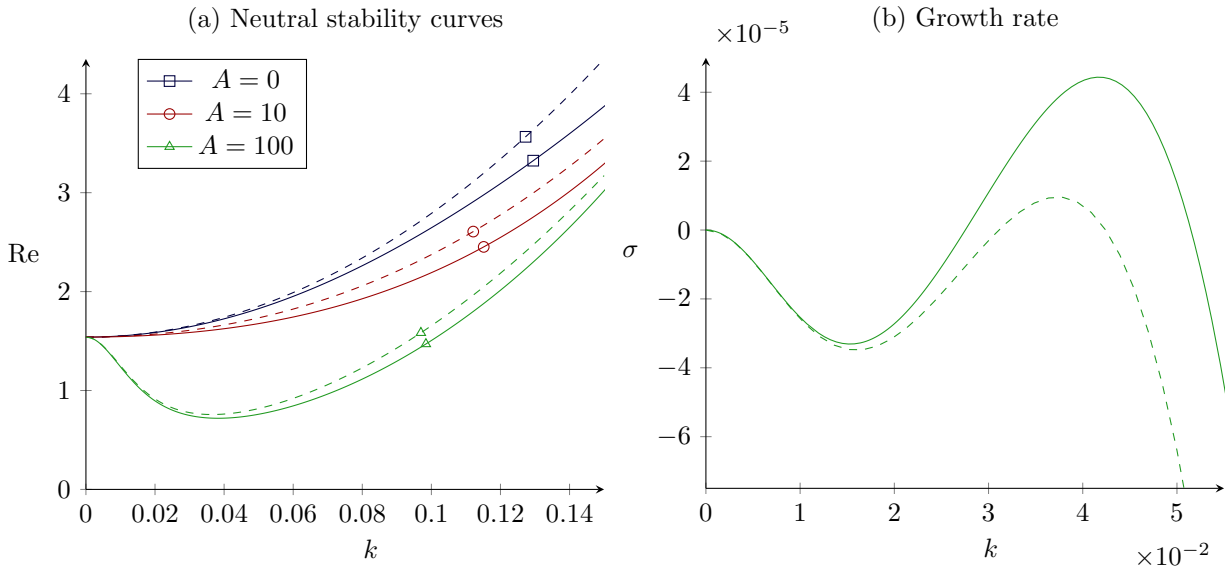

FIG. 2: (a) Neutral stability curves for We = 100, Ma = 15, Ct = $\cot(\pi/12) \approx 3.7$, Bi = 1, $K = 1$, $D = 1$, and various A. Solid lines originate from the numerical solution of the OS problem (12), while dashed lines are from numerical solution of the eigenvalue equation (28) for the WRIBL model with single sine term representation of the temperature correction. In each case the Reynolds number at $k = 0$ is Re_0. For sufficiently large A, the neutral curve becomes non-monotonic, implying that instability first occurs for a critical Reynolds number Re_c less than Re_0, and this instability occurs at a finite wavelength. (b) The growth rate σ for parameters as above, with $A = 100$ and Re = 0.77, showing the finite-wavelength instability. As depicted in both figures, the WRIBL model agrees in the long-wavelength limit, but slightly underestimates the instability compared to the full equations, becoming less accurate as k increases.

Keeping terms to $O(\epsilon)$, the streamwise momentum equation is multiplied by a weight function equal to the leading-order velocity [the first term on the right-hand side of (16)], and then integrated across the depth from $y^+ = 0$ to $y^+ = h$, providing an approximate momentum balance that gives an equation for the evolution of q (the evolution of h in terms of q comes trivially from the mass balance). This approach is equivalent to a Galerkin projection with polynomial basis functions, although here the aim is to use a low-order approximation to analytically derive a reduced-order system, rather than use a higher-order approximation as would be the case in a numerical scheme.

Thus derived, the first-order weighted-residual approximation of (2), (6) is

$$h_t = -q_x, \qquad \frac{6}{5}\mathrm{Re}\left(q_t + \frac{17q}{7h}q_x - \frac{9q^2}{7h^2}h_x\right) + \frac{3q}{h^2} = 2h + 2\mathrm{We}hh_{xxx} - 2hh_x\mathrm{Ct} - 3\mathrm{Ma}\tau_x. \tag{17}$$

We derive an equation for the surface temperature $\tau(x,t)$ from the energy equation (4) by using a similar weighted-residual approach. Assuming that the Prandtl number Pr is $O(1)$ as already done in the previous section, heat convection in the liquid is neglected in the $O(\epsilon)$ weighted-residual model, and only the leading-order term for the surface temperature τ in ϵ is required in (17). Diffusion in the solid is formally included at this order given $A = O(\epsilon^{-1})$, in which case the leading-order problem for the heat equation is

$$T^+_{y^+y^+} = 0, \qquad T^-_{y^-y^-} = AT^-_t, \tag{18}$$

with boundary conditions as in (8). As before, ϵ has been eliminated by scaling x and t. We must also assume $D \ll \epsilon^{-1}$ in order to neglect conduction along the wall in the x-direction; this will not be valid if the wall is sufficiently thick. The Biot numbers K and Bi, that appear in the boundary conditions, are also taken to be $O(1)$.

Unlike the infinite-diffusivity case ($A = 0$), the solution to (18), and thus the surface temperature τ, cannot be represented exactly as a function of h. Instead, we derive an approximate equation for the surface temperature, based on a Fourier series solution to the heat equation and in the same spirit as for the weighted-residual approach used to derive (17). Since the leading-order temperature in the fluid layer is linear,

$$T^+ = T_w\frac{\mathrm{Bi}(h - y^+) + 1}{\mathrm{Bi}h + 1}, \qquad 0 < y^+ < h, \tag{19}$$

the heat equation for $T^- = T^-(x, y^-, t)$ in the solid has a time-dependent Robin condition on $y^- = 0$ as well as a Dirichlet condition on $y^- = -1$:

$$T^-(x, -1, t) = 1, \qquad T^-_{y^-}(x, 0, t) = -\frac{\mathrm{Bi}K}{\mathrm{Bi}h + 1} T^-(x, 0, t). \tag{20}$$

This is the converse of the situation in the OS linear stability analysis; there, the exact (spectral) solution of the heat equation for the linear correction to T^- resulted in a Robin condition on the amplitude of the correction to T^+. The difficulty of the problem here is due to the coefficient in the boundary condition that depends on h, which is a function of time. If h were constant, the appropriate eigenfunction expansion for T^- would be

$$T^-(x, y^-, t) = 1 - \frac{\mathrm{Bi}K(y^- + 1)}{1 + \mathrm{Bi}(h + K)} + \sum_{n=1}^{\infty} \alpha_n(x, t) \sin(\lambda_n(y^- + 1)), \tag{21}$$

where λ_n's are the positive solutions to

$$\lambda + \frac{\mathrm{Bi}K}{\mathrm{Bi}h + 1} \tan\lambda = 0, \tag{22}$$

and α_n's satisfy $\alpha_{nt} = -\lambda_n^2 \alpha_n / A$. For $h = h(x, t)$, however, substituting the assumed form (21) into the heat equation results in additional terms from the time-dependence of h and λ_n. This is no longer separable, but an approximation may be made by assuming a single Fourier mode and computing the evolution equation for the coefficient of this mode. We thus assume the approximate form for T^-:

$$T^- \approx \hat{T}^- = 1 - \frac{\mathrm{Bi}K(y^- + 1)}{1 + \mathrm{Bi}(h + K)} + \alpha(x, t) \frac{\mathrm{Bi}h + 1}{\sin(\lambda)} \sin(\lambda(y^- + 1)) \tag{23}$$

where λ is the smallest positive root of (22) (thus $\pi/2 < \lambda < \pi$). The factors in the last term are chosen so that the surface temperature is given by

$$\tau = \frac{\hat{T}^-(x, 0, t)}{\mathrm{Bi}h + 1} = \frac{1}{1 + \mathrm{Bi}(h + K)} + \alpha, \tag{24}$$

thus α is the deviation from the (h-dependent) surface temperature given by the straight-line temperature profile.

The definition of λ implies that $\hat{T}^-$ in (23) exactly satisfies the temperature and flux boundary conditions, and the only approximation is in satisfying the governing equation itself. As with the derivation of (17), we minimize the residual weighted by the basis function itself, that is, set

$$\int_{-1}^{0} (\hat{T}^-_{y^-y^-} - A\hat{T}^-_t) \sin(\lambda(y^- + 1))\, \mathrm{d}y^- = 0, \tag{25}$$

which results in the following equation for α_t:

$$\alpha_t = [-C_1(h) + C_2(h)\alpha]h_t - C_3(h)\alpha, \tag{26a}$$

where the coefficients are

$$C_1 = \frac{2\mathrm{Bi}\Lambda}{[1 + \mathrm{Bi}(h + K)][\mathrm{Bi}K + (\mathrm{Bi}h + 1)\Lambda]}, \tag{26b}$$

$$C_2 = \frac{\mathrm{Bi}\Lambda[\mathrm{Bi}K - (1 + \mathrm{Bi}h + 2\mathrm{Bi}K)\Lambda]}{2[\mathrm{Bi}K(\mathrm{Bi}h + 1)\Lambda]^2} + \frac{\mathrm{Bi}^2\Lambda K}{(\mathrm{Bi}h + 1)[\mathrm{Bi}K + (\mathrm{Bi}h + 1)\Lambda]} - \frac{\mathrm{Bi}}{\mathrm{Bi}h + 1}, \tag{26c}$$

$$C_3 = \frac{\mathrm{Bi}^2K^2}{(\mathrm{Bi}h + 1)^2 A} \frac{1 - \Lambda}{\Lambda}, \tag{26d}$$

and we have defined $\Lambda = \cos^2\lambda > 0$ (further calculations are included in Appendix A). Note that C_1 and C_3 are both positive, while C_2 could be positive or negative. Given the surface temperature (24), the evolution equations are now

$$h_t = -q_x \tag{26e}$$

$$\frac{6}{5}\mathrm{Re}\left(q_t + \frac{17q}{7h}q_x - \frac{9q^2}{7h^2}h_x\right) + \frac{3q}{h^2} = 2h + 2\mathrm{We}hh_{xxx} - 2hh_x\mathrm{Ct} + 3\mathrm{Ma}\left(\frac{\mathrm{Bi}h_x}{[1 + \mathrm{Bi}(h + K)]^2} - \alpha_x\right). \tag{26f}$$

B. Linear stability

It is important to determine how well the above model of heat transport captures the linear stability characteristics of the full problem (15a). To compare, we determine the linear stability of (26) near the steady-state solution $h = 1$, $q = 2/3$, $\alpha = 0$. Let $h \sim 1 + \tilde{h}\mathrm{e}^{\mathrm{i}k(x-ct)}$, $q \sim 2/3 + \tilde{q}\mathrm{e}^{\mathrm{i}k(x-ct)}$ and $\alpha \sim \tilde{\alpha}e^{\mathrm{i}k(x-ct)}$. Linearizing (26e) and (26a), we express the flux and heat correction amplitudes $\tilde{q}$ and $\tilde{\alpha}$ in terms of $\tilde{h}$:

$$\tilde{q} = \frac{\tilde{h}}{c}, \qquad \tilde{\alpha} = \frac{\mathrm{i}ckC_1(1)\tilde{h}}{C_3(1) - \mathrm{i}ck}. \tag{27}$$

Upon substitution into (26f), we find the eigenvalue equation for c in terms of k:

$$\begin{aligned} &\frac{6}{5}\mathrm{Re}\left(-\mathrm{i}c^2k + \frac{34}{21}\mathrm{i}ck - \frac{4}{7}\mathrm{i}k\right) + 3c - 6 \\ &\quad = -2\mathrm{i}k^3\mathrm{We} - 2\mathrm{i}k\mathrm{Ct} + 3\mathrm{i}k\mathrm{Ma}\left(\frac{\mathrm{Bi}}{[1+\mathrm{Bi}+\mathrm{Bi}K]^2} - \frac{\mathrm{i}ckC_1(1)}{C_3(1)-\mathrm{i}ck}\right). \end{aligned} \tag{28}$$

We take the long-wave expansion near $k = 0$, as was done for the OS system (12). Again we compute the long-wave behavior of the neutral curve $\mathrm{Re} = \mathrm{Re}^*(k)$ by expanding $\mathrm{Re}^* \sim \mathrm{Re}_0 + k^2\mathrm{Re}_2$, $c \sim c_0 + k^2c_2$. The result of this expansion is

$$\mathrm{Re}_0 = \frac{5}{4}\mathrm{Ct} - \frac{15}{8}\frac{\mathrm{MaBi}}{[1+\mathrm{Bi}+\mathrm{Bi}K]^2}, \tag{29}$$

$$\mathrm{Re}_2 = \frac{5}{4}\mathrm{We} - \frac{15}{2}\frac{\mathrm{Ma}C_1}{C_3^2} + \frac{125\mathrm{Ma}C_1}{28C_3}\left(\frac{3}{2}\frac{\mathrm{MaBi}}{[1+\mathrm{Bi}+\mathrm{Bi}K]^2} - \mathrm{Ct}\right). \tag{30}$$

The leading-order term Re_0 in (29) is identical to the critical Reynolds number predicted by the OS analysis (15b). A direct comparison between the k^2 terms (30) and (15c) is impossible due to the transcendental equation for $\Lambda_0 = \Lambda|_{h=1}$. An approximate comparison may be made in certain asymptotic limits, for instance, for small Bi. In this case, the approximate solution to (22) for $h = 1$ is

$$\lambda \sim \frac{\pi}{2} + \frac{2}{\pi}\mathrm{Bi}K, \tag{31}$$

thus $\Lambda_0 \sim 4\mathrm{Bi}^2K^2/\pi^2$, $C_1(1) \sim 8\mathrm{Bi}^2K/\pi^2$ and $C_3(1) \sim \pi^2/(4A)$. Substituting into Re_2 in (30) and keeping terms of order We or A^2 results in

$$\mathrm{Re}_2 \sim \frac{5}{4}\mathrm{We} - \frac{960}{\pi^6}\mathrm{Bi}^2KA^2\mathrm{Ma} \tag{32}$$

Note $960/\pi^6 \approx 0.999$, so this result is very close to the small-Bi limit of the result from the OS analysis (15c).

The neutral and growth rate curves of the reduced-order model are compared with the OS results in Fig. 2. The reduced-order model is clearly exact in the long-wavelength limit $k \to 0$, and the second derivative at $k = 0$ (corresponding to Re_2) is also negative when $A = 100$. Of course, the reduced-order model becomes less accurate as k increases, as is also the case for an isothermal falling film [4] but importantly, it qualitatively captures the non-monotonicity of the neutral curve $\mathrm{Re}^*(k)$, and thus the appearance of a finite-wavelength instability, as A increases.

C. Parameter ranges where short-wave instability is possible

For short-wave instability to occur for $\mathrm{Re}_c < \mathrm{Re} < \mathrm{Re}_0$, we require $\mathrm{Re}_0 > 0$ and $\mathrm{Re}_2 < 0$. From the expressions for these quantities in (29), (30) it follows that we must have

$$\frac{5}{4}\mathrm{We} - \frac{15}{2}\frac{\mathrm{Ma}C_1}{C_3^2} < 0. \tag{33}$$

Substituting expressions (26b) and (26d) for C_1 and C_3, and using (22) to explicitly write K in terms of λ, the above inequality becomes

$$\begin{aligned} \frac{\mathrm{We}}{A^2\mathrm{Ma}} &< \frac{12\Lambda^3(1+\mathrm{Bi})^4}{\mathrm{Bi}^3K^4(1-\Lambda)^2(1+\mathrm{Bi}+\mathrm{Bi}K)(\Lambda+\Lambda\mathrm{Bi}+\mathrm{Bi}K)} \\ &= \frac{12\mathrm{Bi}}{(1+\mathrm{Bi})^2}\frac{\sin^6\lambda\cos\lambda}{\lambda^4(\sin\lambda\cos\lambda-\lambda)(\sin\lambda-\lambda\cos\lambda)} = \mathcal{G}(\mathrm{Bi},\lambda). \end{aligned} \tag{34}$$

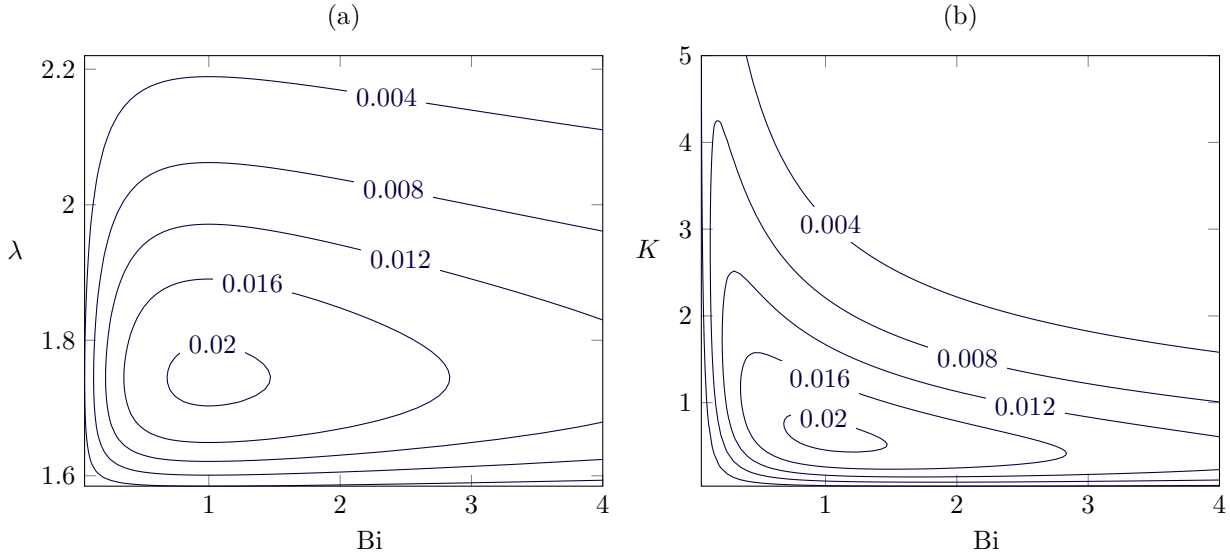

FIG. 3: Contours of the function $\mathcal{G}$ defined in (34), in (a) the (Bi, λ)-plane and (b) the (Bi, K)-plane. The interior of the level curves denotes the region where short-wave instability may occur; the appropriate level curve is determined by the values of We, Ma and A according to (34).

For given $\mathrm{We}/(A^2\mathrm{Ma}) = r$, the r-level curve of $\mathcal{G}$ represents the borderline between parameter regions where short-wave mode is possible, and where it is not. In Fig. 3, we plot these level curves in the (Bi, λ)- and (Bi, K)-planes, see panels (a) and (b), respectively. We note that $\mathcal{G}$ has an interior maximum; as the dependence on Bi and λ is separable, it is easy to see that this maximum occurs when $\mathrm{Bi} = 1$, while the numerically computed optimum value for λ is

$$\lambda_{\max} \approx 1.75 \;\Rightarrow\; K_{\max} \approx 0.613, \quad \mathcal{G}_{\max} = \mathcal{G}(1, \lambda_{\max}) \approx 0.0208. \tag{35}$$

Thus if $\mathrm{We}/(A^2\mathrm{Ma}) > 0.0208$, the short-wave instability cannot be present.

While this analysis provides a necessary condition for a short-wave mode, sufficient conditions are much harder to determine. If $\mathrm{We}/(A^2\mathrm{Ma}) < 0.0208$, the short-wave instability will exist only if (Bi, K) lie within the appropriate region, and Ct is such that $\mathrm{Re}_0 > 0$ but Re_2 remains negative. Finally, Re must be less than Re_0 but greater than the critical Reynolds number Re_c, the minimum in the curve $\mathrm{Re}^*(k)$.

V. TRAVELING-WAVE COMPUTATIONS

We now examine traveling-wave solutions to (26). As well as exploring the quantitative effect of A on the shape and speed of the waves, we also examine the quantitative effect of $A > 0$ on the bifurcation structure of the associated dynamical system. Lastly, we find the bifurcations that lead to non-trivial periodic solutions for $\mathrm{Re}_c < \mathrm{Re} < \mathrm{Re}_0$ when A is sufficiently large, corresponding to the short-wave instability uncovered in the linear stability analysis.

As is standard, traveling-wave solutions which are stationary in a frame moving with speed c are found by letting $z = x - ct$ be the independent variable, and writing the system (26) as a system of ordinary differential equations. Integrating the continuity equation (26e) once results in $q = ch + C_0$, where C_0 is the flux in the traveling reference frame. For solitary pulses, we will demand $h \to 1, q \to 2/3$ in the far field, thus $C_0 = 2/3 - c$. Solving (26f) for the third derivative and (26a) for the derivative of α results in

$$h''' = \mathcal{F}(c,h) - \left(\mathcal{R}(c,h) + \mathcal{M}[C_1(h) - C_2(h)\alpha]\right) h' + \mathcal{M}(h)\frac{C_3(h)}{c}\alpha, \tag{36a}$$

$$\alpha' = (-C_1(h) + C_2(h)\alpha)h' + \frac{C_3(h)}{c}\alpha, \tag{36b}$$

where dashes denote differentiation with respect to z, and

$$\mathcal{R}(c,h) = \frac{3\mathrm{Re}}{5\mathrm{We}h}\left(c^2 - \frac{17c[c(h-1)+2/3]}{7h} + \frac{9[c(h-1)+2/3]^2}{7h^2}\right) - \frac{\mathrm{Ct}}{\mathrm{We}} + \frac{3\mathrm{Ma}}{2h\mathrm{We}}\frac{\mathrm{Bi}}{(1+\mathrm{Bi}h+\mathrm{Bi}K)^2}, \tag{36c}$$

$$\mathcal{F}(c,h) = \frac{(h-1)[3c-2(h^2+h+1)]}{2\mathrm{We}h^3}, \tag{36d}$$

$$\mathcal{M}(h) = \frac{3\mathrm{Ma}}{2\mathrm{We}h}. \tag{36e}$$

A. Numerical method

The numerical computation of bifurcations and solutions of (36) is performed again using AUTO07p [40]. Given that $\lambda = \lambda(h)$ is only implicitly defined through (22), it is easier to treat λ as the state variable, from which h can be computed. From (22), we find

$$\lambda' = -\frac{\mathrm{Bi}\lambda h'}{1+\mathrm{Bi}h+\mathrm{Bi}K/\Lambda}, \qquad h = -\frac{1}{\mathrm{Bi}}\left(1+\mathrm{Bi}K\frac{\tan\lambda}{\lambda}\right). \tag{37}$$

In the numerical scheme, we thus define the state variable vector to be $\boldsymbol{V} = [\lambda\ h'\ h''\ \alpha]^T$. We report our results in terms of h, however, for ease of interpretation.

B. Bifurcations from the trivial state

We define the state-space vector $\boldsymbol{U} = [h\ h'\ h''\ \alpha]^T$. At equilibrium, $h' = h'' = 0$ and $\alpha = 0$ from (36b). Requiring $h''' = 0$ in (36a) demands $\mathcal{F}(c,h) = 0$, thus (36) has three equilibrium points $\boldsymbol{U}_j$:

$$\boldsymbol{U}_j = [h_j\ 0\ 0\ 0]^T, \qquad h_0 = 1,\ h_{1,2} = \tfrac{1}{2}(-1 \pm \sqrt{6c-3}), \tag{38}$$

where the h_j's are the three roots of $\mathcal{F}(c,h)$.

Solitary pulses correspond to homoclinic orbits connecting $\boldsymbol{U}_0$, while periodic waves correspond to limit cycles near this point. While we are not interested in orbits involving the other two equilibrium points, $\boldsymbol{U}_1$ plays an important role in the bifurcation that leads to long waves, as we expand upon below (h_2 is always negative, so $\boldsymbol{U}_2$ is not important).

Linearizing (36) around $\boldsymbol{U}_j$ results in the Jacobian matrix

$$J = \begin{bmatrix} 0 & 1 & 0 & 0 \\ 0 & 0 & 1 & 0 \\ \mathcal{F}_h & -(\mathcal{R}+\mathcal{M}C_1) & 0 & \mathcal{M}C_3/c \\ 0 & -C_1 & 0 & C_3/c \end{bmatrix}$$

(dependence of $\mathcal{F}_h$, $\mathcal{R}$, $\mathcal{M}$, $\mathcal{C}_1$, and $\mathcal{C}_3$ on c and $h = h_j$ has been suppressed for clarity). The characteristic polynomial p of J is

$$p(\mu) = \left[\mu^3 + \mathcal{R}\mu - \mathcal{F}_h\right] - \frac{c}{C_3}\left[\mu^4 + (\mathcal{R}+\mathcal{M}C_1)\mu^2 - \mathcal{F}_h\mu\right]. \tag{39}$$

Given the linear stability properties of the WRIBL model in Sec. IV, if the Reynolds number is supercritical [corresponding to $\mathcal{R} > 0$ in (36)], then we expect a bifurcation from the flat film to traveling-wave solutions at the linear wave speed $c = 2$. Indeed, at this wave speed $\mathcal{F}_h(2,h) = 0$ and J has a zero eigenvalue corresponding to the transcritical bifurcation caused by the collision of $\boldsymbol{U}_0$ and $\boldsymbol{U}_1$. In the limit of infinite substrate diffusivity ($A \to 0$), $C_3 \to \infty$ and so there is also a Hopf bifurcation at $c = 2$ ($\mu = \pm\mathrm{i}\sqrt{\mathcal{R}(2)}$). This simultaneous bifurcation had been referred to as a *Gavrilov–Guckenheimer* point [4, 42, 43], and is known to arise in the isothermal Benney equation [4] as well as the Kuramoto–Sivashinsky equation [44], which is an approximation of the isothermal falling film near the critical Reynolds number [4].

Including the substrate diffusivity has the effect of separating the transcritical and Hopf bifurcations. Two Hopf bifurcations result, one on each branch $\boldsymbol{U}_0$ and $\boldsymbol{U}_1$. To estimate the location of the Hopf bifurcation on $\boldsymbol{U}_0$ (on which

$h = 1$) for small but finite A, we consider $C_3(2,1)^{-1}$ to be a small parameter (recall that $C_3 \propto 1/A$), and expand $\mu \sim \mathrm{i}\sqrt{R(2,1)} + \mathrm{i}C_3(2,1)^{-1}\tilde{\nu}$ and $c = c_0^{\mathrm{hopf}} \sim 2 + C_3(2,1)^{-1}\tilde{c}$ into (39), where $\tilde{\nu}$ and $\tilde{c}$ are real (the Hopf bifurcation is characterized by imaginary μ). The correction $\tilde{c}$ to the speed at which the Hopf bifurcation occurs is determined by solving the real part of (39) at order $C_3(2,1)^{-1}$:

$$\Re(\mu^3 + \mathcal{R}\mu - \mathcal{F}_h) \sim -\frac{\mathcal{F}_{ch}(2,1)\tilde{c}}{C_3(2,1)} = -\frac{3\tilde{c}}{2C_3(2,1)\mathrm{We}} \tag{40}$$

$$\Re\left(\frac{c}{C_3}\left[\mu^4 + (\mathcal{R} + \mathcal{M}C_1)\mu^2 - \mathcal{F}_h\right]\right) \sim -\frac{2\mathcal{M}(1)C_1(2,1)\mathcal{R}(2,1)}{C_3(2,1)} = -\frac{4}{3}\frac{\mathrm{Ma}C_1(2,1)\mathcal{R}(2,1)}{C_3(2,1)\mathrm{We}} \tag{41}$$

By solving for $\tilde{c}$ by equating (40) and (41), and then substituting the result into the assumed form for c_0^{hopf}, we thereby obtain the approximation

$$c_0^{\mathrm{hopf}} \sim 2 + \frac{2\mathrm{Ma}C_1(2,1)\mathcal{R}(2,1)}{C_3(2,1)} > 2, \qquad A \ll 1. \tag{42}$$

For finite diffusivity, the Hopf bifurcation on $\boldsymbol{U}_0$ occurs at $c > 2$.

To estimate the location of the Hopf bifurcation on $\boldsymbol{U}_1$ (on which $h = h_1$) for small but finite A, we must also expand h_1 in large C_3. Similar to before, we expand $\mu \sim \mathrm{i}\sqrt{R(2,1)} + \mathrm{i}\delta\tilde{\nu}$ and $c = c_1^{\mathrm{hopf}} \sim 2 + \delta\tilde{c}$. Defining $h_1 \sim 1 + \delta\tilde{h}$, from (38) we find $\tilde{h} = \tilde{c}/2$. Now the only change for the analysis on h_0 is that (40) is replaced with

$$\Re(\mu^3 + \mathcal{R}\mu - \mathcal{F}_h) \sim -\frac{\mathcal{F}_{ch}(2,1)\tilde{c} - F_{hh}(2,1)\tilde{h}}{C_3(2,1)} = \frac{3\tilde{c}}{2C_3(2,1)\mathrm{We}}. \tag{43}$$

Equating (41) and (43) and solving for $\tilde{c}$ results in

$$c_1^{\mathrm{hopf}} \sim 2 - \frac{2\mathrm{Ma}C_1(2,1)\mathcal{R}(2,1)}{C_3(2,1)} < 2, \qquad A \ll 1. \tag{44}$$

Thus the Hopf bifurcation on $\boldsymbol{U}_1$ occurs at $c < 2$.

We now use numerical continuation to follow the branch of periodic orbits originating from each Hopf bifurcation. As the period increases without bound, the orbit approaches a homoclinic orbit (that is, a global homoclinic bifurcation); however, the equilibrium point connected by this homoclinic orbit is not necessarily the one from which the periodic solutions bifurcated.

In Fig. 4(a), we plot the result of this numerical continuation for $A = 10$. It is in fact the branch originating at the Hopf bifurcation on h_1 that tends to a homoclinic orbit connecting $h_0 = 1$, via an exponential snaking behavior. This branch exists at wave speeds $c < 2$, and the homoclinic orbit approached corresponds to an inverted pulse [representative solutions are shown in Fig. 6(e)]. The branch originating on $h_0 = 1$, $c > 2$ does not tend to a homoclinic orbit connecting h_0 (in fact, numerically we had difficulty increasing the period much beyond a certain point).

In order to compute pulses for $c > 2$, we introduce an artificial dispersion parameter δ into the model by altering (36a) as follows:

$$h''' = \mathcal{F}(c,h) - (\mathcal{R}(c,h) + \mathcal{M}[C_1(h) - C_2(h)\alpha])\,h' + \mathcal{M}(h)\frac{C_3(h)}{c}\alpha - \delta h''. \tag{45}$$

The additional term $-\delta h''$ is a linearized version of the viscous dispersion term included in the simplified second-order WRIBL model [31–33]. Including this term with $\delta > 0$ also has the effect of separating Hopf bifurcations from the transcritical bifurcation [4]. However, now the Hopf bifurcation on h_1 occurs at $c > 2$, and the branch of periodic orbits that emanates from this bifurcation tends toward a homoclinic bifurcation at h_0, which corresponds to a forward pulse [see Fig. 6(c)]. This bifurcation structure is plotted in Fig. 4(b) with $\delta = 1$. The branch originating from the Hopf bifurcation on h_0 tends to a homoclinic bifurcation at h_1; the form of the traveling wave solution at the homoclinic bifurcation is also that of a forward pulse, but scaled to a smaller value of the mean thickness (and thus lower wave speed).

Solutions to the original problem may now be found numerically by homotopy continuation, starting with $(\delta, \mathrm{Ma}) = (1, 0)$, increasing the period to find the traveling-pulse solution, then decreasing δ to zero and increasing Ma from zero to reintroduce thermal effects.

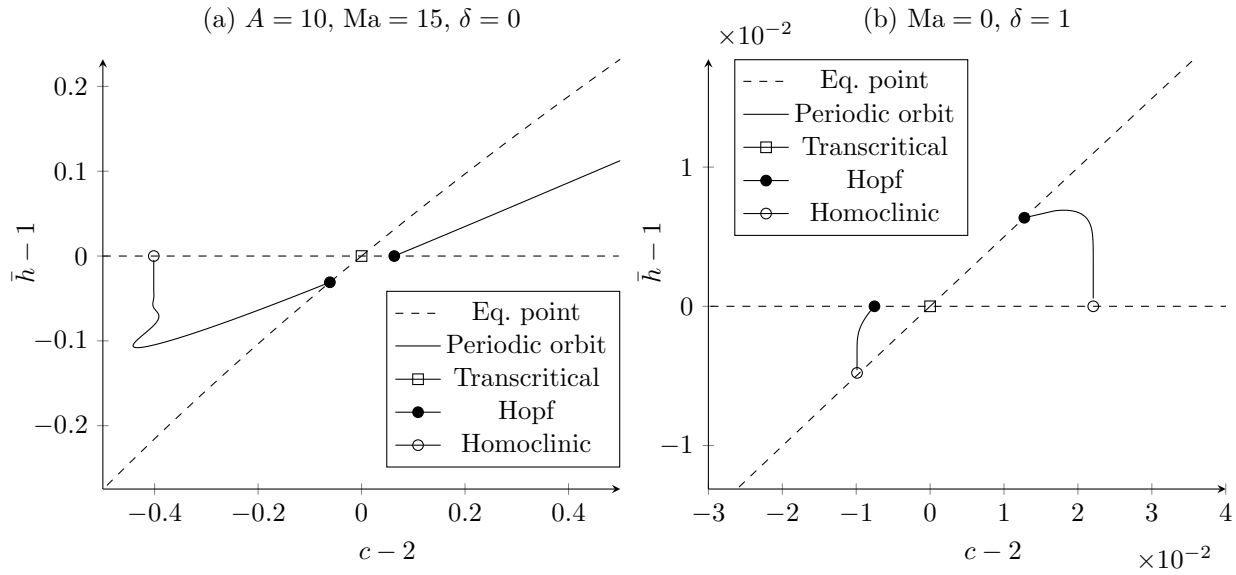

FIG. 4: Hopf bifurcations near the transcritical bifurcation at the linear wave speed $c = 2$. (a) $A = 10$, Ma $= 15$, $\delta = 0$: By plotting the mean thickness $\bar{h}$ against wavespeed c, the branch originating from the Hopf bifurcation on h_1 is seen to tend, via a global homoclinic bifurcation, to a homoclinic orbit connecting $h_0 = 0$, corresponding to an inverse pulse with $c < 2$. (b) Ma $= 0$, $\delta = 1$: introducing an artificial dispersive-like term and removing the effect of heat changes the position of the Hopf bifurcations. The periodic orbits originating at the bifurcation point on h_1 tend to a homoclinic orbit connecting $h_0 = 0$, corresponding to a forward pulse. The dispersion may then be removed and heat reintroduced by homotopy continuation.

The other bifurcations of interest are those that correspond to a short-wave instability when Re is subcritical and A is large. We do not attempt to analyze the linearized dynamical system at these points, but the results from the stability analysis strongly indicate that these are isolated Hopf bifurcations that occur at a value of $c > 2$. We verify this with numerical computations. In Fig. 5(a), we plot the bifurcation structure. There are now two Hopf bifurcations on each branch h_0 and h_1. Numerical continuation shows that each of these Hopf pairs are connected, that is, the period may not be increased indefinitely to find a homoclinic orbit, but only periodic solutions exist in this parameter regime. In Fig. 5(b), we plot the deviation of the wave speed from the linear speed 2 against the wavenumber (equal to 2π divided by the period) for the branch connected to h_0; the wavenumber at each end corresponds to the cutoff wavenumbers from the linear stability analysis [see Fig. 2(b)]. Lastly, in Fig. 5(c) we plot each of the state variables $[h, h', h'', \alpha]$ at the turning point $k = 3.93 \times 10^{-2}$, $c - 2 = 9.38 \times 10^{-3}$ on this branch ; while h superficially appears sinusoidal, the nonlinearity is apparent in the higher derivative terms.

C. Branches of solitary pulses

We now trace out branches of solitary pulses (homoclinic orbits) by using numerical continuation to vary Re both up and down, allowing the wave speed c to vary. We adopt the two starting points found using the methods of the previous section; for $c > 2$, we start with a large value of Re and the homotopy approach to include and then remove dispersion, while for $c < 2$, we start at a solution with Re close to criticality, found by continuation in the period from the Hopf bifurcation depicted in Fig. 4(a).

In Fig. 6, we plot the branches thus computed, for $A = 0, 10, 100$, and other parameters as listed in the caption of Fig. 2. The upper branch ($c > 2$) corresponds to single-hump pulses as depicted in Fig. 6(c) for Re $= 5$. The effect of increasing A (decreasing substrate diffusivity) for large Re is to slightly increase the wave amplitude and speed, and to smear out the wall temperature; the temperature exhibits a long tail behind the pulse, due to the transient heat storage in the wall. As Re is decreased, the branch does not connect to the point $(\mathrm{Re}, c) = (\mathrm{Re}_0, 2)$, unless $A = 0$. Instead, it has a turning point and merges with a branch of double-hump pulses with $c > 2$; see Fig. 6(d). For $A = 0$, it is expected that both of these branches exist (and an infinite number of others, due to a theorem by Shilnikov [4, 43, 45]) and connect to $(\mathrm{Re}_0, 2)$, so increasing A has the effect of merging these two branches. The fate of other multi-hump solution branches is beyond the current numerical study.

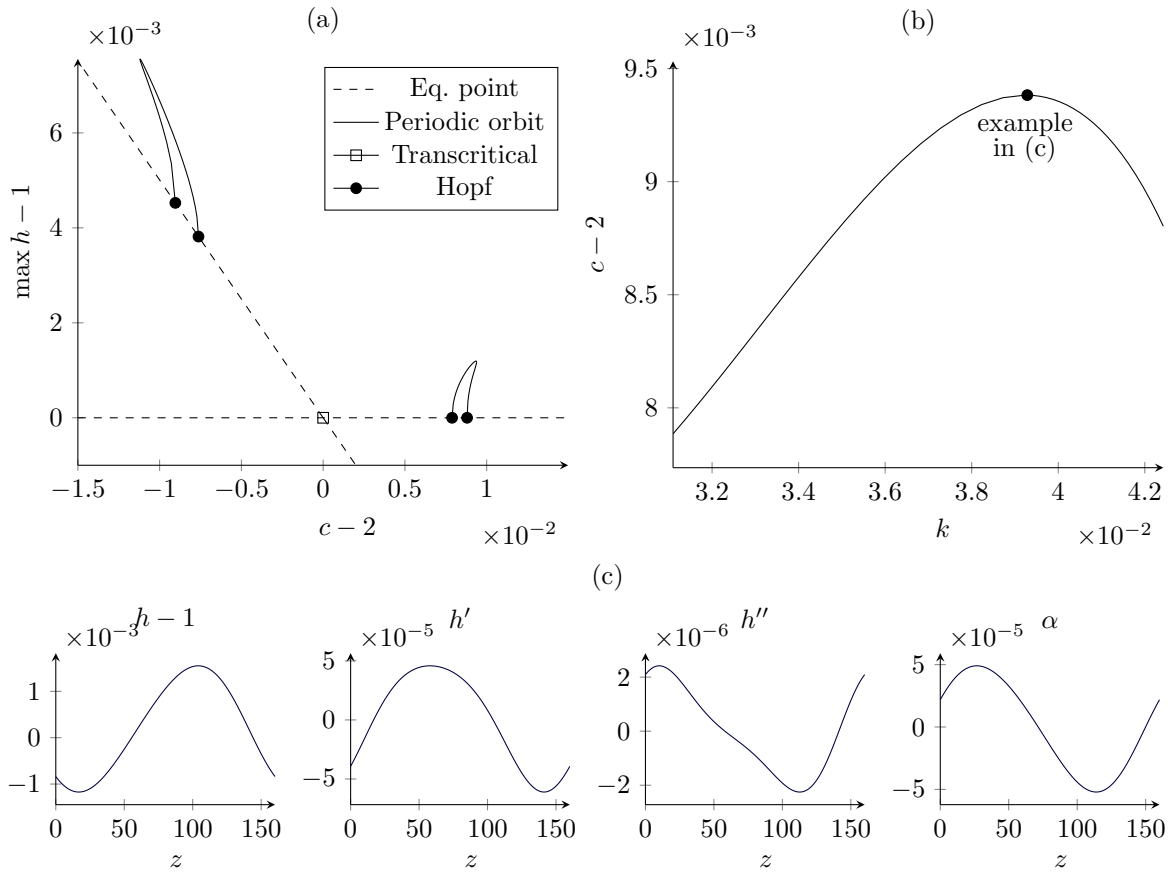

FIG. 5: Hopf bifurcations near the linear wave speed $c = 2$ for $A = 100$ and subcritical Reynolds number $\mathrm{Re} = 0.77$. (a) At these values, the short wave instability leads to the existence of a branch of periodic solutions connected to the trivial uniform state by a pair of Hopf bifurcations. (b) The wavenumber on the branch connected to $h_0 = 1$ varies between the two critical wavenumbers predicted by the linear stability analysis. (c) The state variables $[h, h', h'', \alpha]^T$ at the marked point $k = 3.93 \times 10^{-2}$, $c - 2 = 9.38 \times 10^{-3}$ on the periodic branch depicted in (b). The nonlinearity can be seen in the higher derivatives.

The lower branch ($c < 2$) of solutions does connect to $(\mathrm{Re}_0, 2)$, as may be expected from the bifurcation analysis of the previous section. This branch represents negative-hump pulses as depicted in Fig. 6(e). The effect of increasing A is to increase the amplitude but decrease the speed of pulses. Again, the wall temperature exhibits a long tail for large A.

Finally, we note that for large A, the solitary-pulse branches may extend to subcritical Reynolds numbers $\mathrm{Re} < \mathrm{Re}_0$ as seen in Figs. 6(a) and 6(b). Recall from Fig. 2 that in this region the flat film is unstable to perturbations in a finite band of wavenumbers away from the zero wavenumber; the connection between these pulse solutions and the periodic solution branches computed in Fig. 5 is not immediately clear, and we do not pursue the issue further in this study.

VI. COMPUTATION OF TIME-DEPENDENT SOLUTIONS

We now compute time-dependent solutions of the WRIBL model (26). Again, as the film thickness h is an explicit function of the eigenvalue λ that appears in the equation for α, the simplest numerical approach is to treat (λ, q, α) as dependent variables, although for ease of understanding we will report our results in terms of h and wall temperature T_w. In addition, the linear wavespeed $c_0 = 2$ is removed with the transformation $x \mapsto x - 2t$. Spatial derivatives are computed spectrally using the Fast Fourier Transform, while the solution is advanced in time using Matlab's `ode15s` function. For the most part, 256 nodes were used and the solution was continued until $t = 10000$, which took on the order of 10 minutes on a desktop computer.

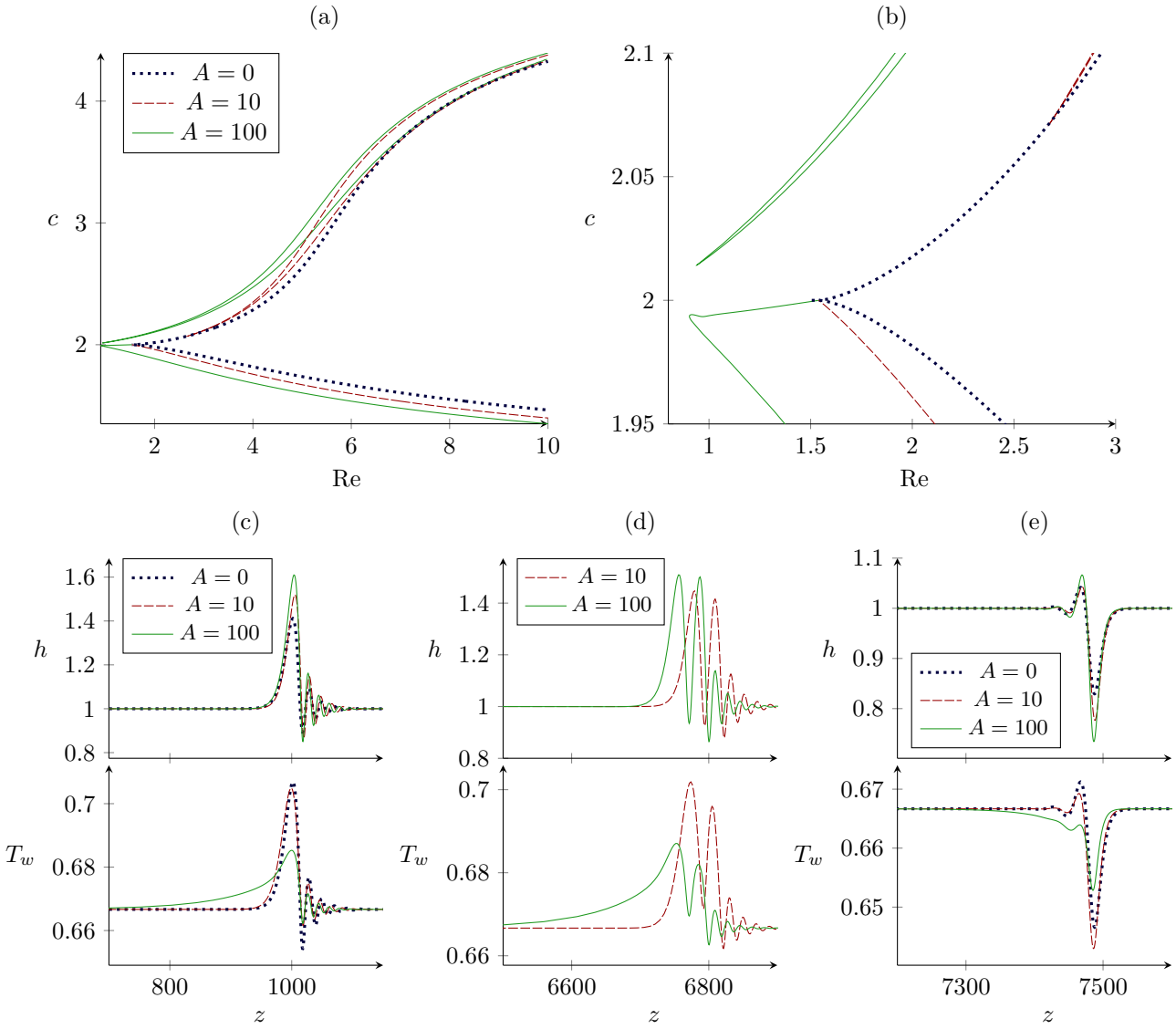

FIG. 6: (a) Speed c vs Reynolds number Re of solitary-pulse solution branches for various values of A. The upper branches with superlinear speed ($c > 2$) are forward pulses as depicted in (c) and (d), and those with sublinear speed ($c < 2$) are negative-hump pulses depicted in (e). Superlinear branches with $A > 0$ do not approach the linear wavespeed, instead exhibiting a turning point at which the single-hump solitary-wave branch merges with a double-hump wave branch. (b) A close up of the traveling-pulse branches near the linear wave speed and long-wave critical Reynolds number Re_0. (c–e) The film thickness h and wall temperature T_w for $\mathrm{Re} = 5$ and each value of A, on the single-hump, double-hump and negative-hump branches, respectively. For ease of interpretation the wall temperature T_w has been post-computed from combining the transient term α with the quasi-steady part via (23).

The results of four numerical computations are depicted in Fig. 7. The first three examples show the development of nonlinear traveling waves from an initial sinusoidally perturbed interface, with supercritical Reynolds number $\mathrm{Re} = 8$, $\mathrm{We} = 100$, $\mathrm{Ma} = 15$, $\mathrm{Ct} = \cot(\pi/12) \approx 3.7$, $\mathrm{Bi} = 1$, $K = 1$, and for each of $A = 0$, 10, and 100. In each case, the interface develops into a train of well separated pulses, with form similar to the single-hump waves depicted in Fig. 6. This strongly indicates that for large Re such waves are stable, while the negative or multi-hump pulses are unstable. These single-hump pulses continuously interact with each other via their tails (for detailed studies of pulse interaction and associated coherent structures theories see, e.g., [33, 46–49]). Considering the fully coupled heat transport problem shows that interfacial waves trigger waves in the wall temperature also. The effect of A on the shape and speed of the traveling waves is the same as that we found in Sec. V; the wave speed and amplitude increases slightly for larger values of A, while the wall temperature develops a slowly decaying tail, as in the traveling-wave

solutions.

Much greater precision was needed to compute the short-wave selection for $A = 100$ near the critical Reynolds number; in this case, we took 512 nodes, and used filtering to remove aliasing errors. The computations were run to $t = 100000$ to check the convergence to a non-flat surface. The thickness does indeed converge to a near-sinusoidal periodic wave train, as does the wall temperature.

VII. DISCUSSION

Using linear stability analysis of the full NS/energy equations, and by deriving an appropriate low-dimensional WRIBL model, we have explored the effect of substrate heat flow, in particular finite substrate diffusivity, on the dynamics of falling films affected by thermocapillary surface stresses induced by the wall heating. In both the NS/energy and reduced-order model, decreasing the substrate diffusivity generally leads to increased instability, traveling waves of greater speed and amplitude, and temperature pulses exhibiting long tails as heat stored in the wall is slowly released. In addition, when the substrate diffusivity is sufficiently small, the flat film is unstable to finite-wavelength perturbations at Reynolds number less than the critical value predicted by the long-wavelength limit. We also examined how the inclusion of substrate diffusivity modifies the bifurcation structure which connects the trivial flat film to traveling periodic waves and solitary pulses. Solitary-pulse-like coherent structure are observed in time-dependent computations, as is the selection of a finite wavelength when the diffusivity is sufficiently small.

Although this study has been theoretical in nature, it is worth considering the experimental implications. Unfortunately, there are as of yet no experimental studies that directly examine the effect of thermocapillarity on two-dimensional solitary-pulse-type structures on thin falling films. Thermocapillary thin-film experiments have been performed that focus on three dimensional structures (that is, including the spanwise direction normal to the flow direction) such as the convection cells that lead to rivulets in the free surface [14, 50, 51]. The heat transfer properties of a wavy film on a heated substrate have also been tested [52–54], although without examining the effect of thermocapillarity on the fluid flow in particular. Experiments on two-dimensional pulses have been restricted to the isothermal case [55, 56], where favorable comparisons of the wave speed and profile have been made between experiments, computations of the full Navier–Stokes system, and reduced-order (WRIBL) models. In these experiments, waves are created by flowing liquid down a tilted plate (of about 30 cm length) by oscillating the inlet flux at the upper side of the plate. For appropriate parameters, the periodic waves from the inlet evolve to traveling pulses sufficiently far downstream. In order to include the effect of thermocapillarity in the regime of two-dimensional pulses, resistive heating can be applied to the bottom plate if it is made of a conductive material, such as a titanium foil.

The most notable effect of finite thermal conductivity in the substrate will be the presence of a heat pulse in the solid that follows the pulse on the free surface of the film. If the finite diffusivity of the substrate is also appreciable, then our traveling-wave analysis in Sec. V predicts that there will be a smearing out of this heat pulse and a resultant increase in its speed. For an imposed film-surface wave frequency, there will also be a lag in wall temperature compared to heat flux, which is also seen in oscillating compressible gas flows (see Ref. 52, and references therein). This lag appears in our reduced-order heat equation [captured, for example, in the complex (wavenumber-dependent) constant of proportionality relating the perturbations to temperature $\tilde{\alpha}$ and thickness $\tilde{h}$ in the second equation in (27)], and a comparison to experiments is feasible. Since heating substrate materials used in experiments tend to have much higher thermal conductivities than the liquid film, to study the finite substrate diffusion regime, it may be appropriate to construct a bilayer substrate with a conductive layer underneath a more insulating layer, such as glass, which will have thermal properties similar to the fluid.

The most challenging prediction to recover in an experiment will be the short-wave instability, as the parameter regime over which it occurs is quite small (see Sec. IV C). Since this is only likely to be observed after a long time, the thermal conditions would have to be very tightly controlled, while the Reynolds number could be slowly increased, by gradually increasing the angle of the plate θ, from a subcritical value $\mathrm{Re} < \mathrm{Re}_c$ to the regime $\mathrm{Re}_c < \mathrm{Re} < \mathrm{Re}_0$.

In this study, we have used the standard Nusselt scaling, in which all the dimensionless parameters depend on both the typical thickness h_0 and angle θ. In an experimental context, it is useful to separate out these dependencies, as they are the most easy to vary. We include some detail on critical parameters for the long- and short-wave instability using this method in Appendix B.

An aspect of substrate heat transfer neglected in this study is the streamwise (x-) conduction of heat. This is usually neglected by assuming that the liquid film as well as the substrate are thin, but may be important if the substrate is sufficiently thick. This effect would also be important when considering localized heat sources, in which the streamwise temperature gradient within the wall may be large. The smoothing effect of conduction would then be an alternative to the *a priori* smoothed heat sources used in [15, 20], for example. In the framework of a WRIBL model, streamwise conduction would likely result in a non-local term in the wall temperature boundary condition, similar to that which arises in studies of electrified falling films [57]. We leave this as a possible direction of future

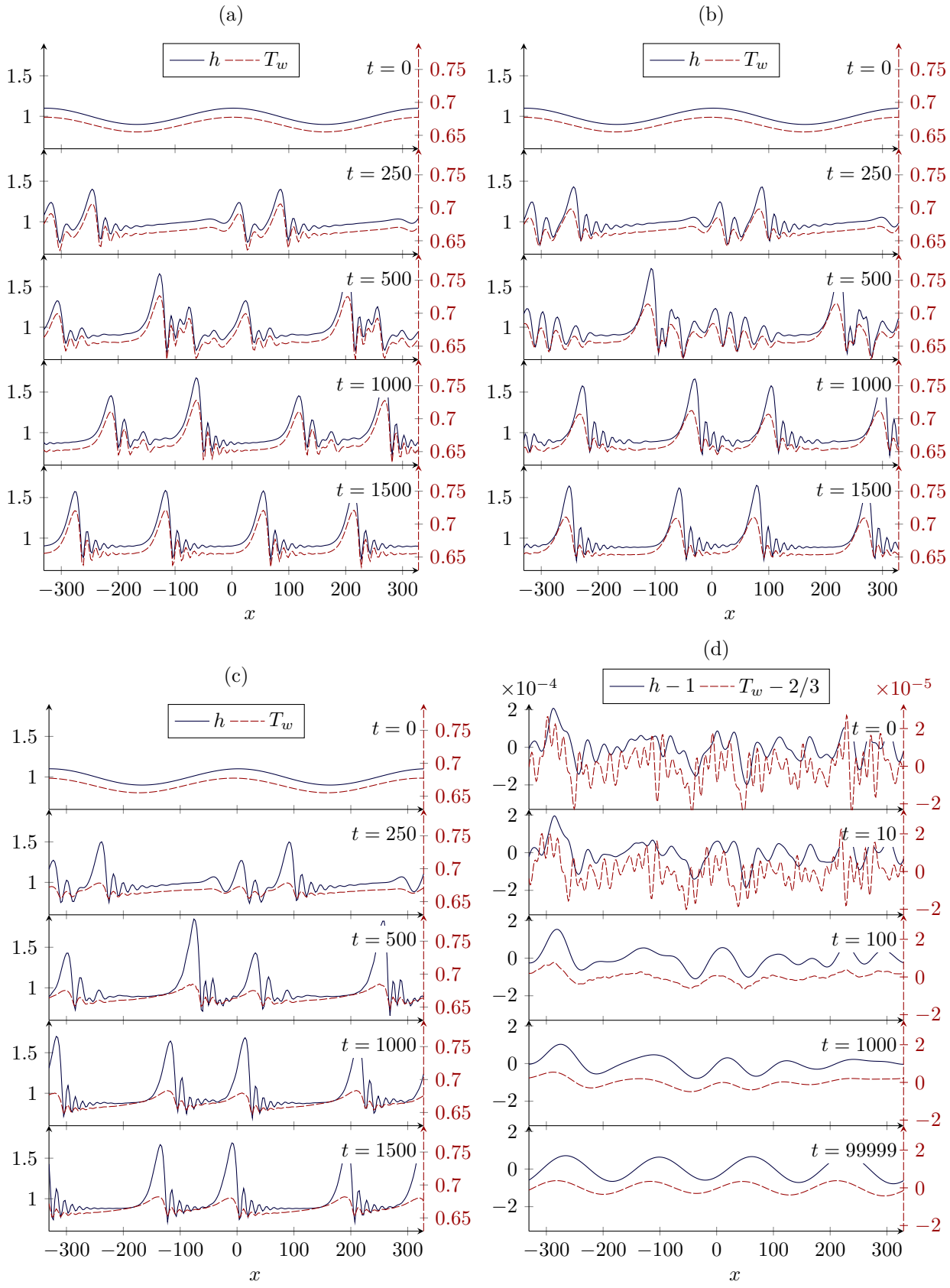

FIG. 7: (continued overleaf)

FIG. 7: Numerical computations show the emergence of traveling-wave structures in the film thickness h and wall temperature T_w from a sinusoidal initial condition for (a) $A = 0$, (b) $A = 10$, and (c) $A = 100$. In each case, $\mathrm{Re} = 8$, and other parameters are as in Fig. 2. For $A = 0$, the pulse in wall temperature closely follows that of film thickness, while for large A, the wall temperature is smoothed out, featuring a large tail in which the temperature slowly decays to its steady value. (d) For $A = 100$ and $\mathrm{Re} = .77$, a noisy initial condition is followed by selection of a finite wavelength, as suggested by the linear stability analysis in Fig. 2.

research.

ACKNOWLEDGMENTS

We acknowledge financial support from the Engineering and Physical Sciences Research Council of the UK through Grants No. EP/K008595/1 and EP/L020564/1. The work of DT was partly supported by EPSRC Grant No. EP/K041134/1. We are grateful to Prof. Benoit Scheid, Université Libre de Bruxelles, and Dr Alexandros Charogiannis, Imperial College London, for numerous stimulating discussions and insightful comments.

Appendix A: Details on equation for transient heat term

To derive (26a), we substitute the assumed form of the temperature profile (23) into the weighted integral (25), and find

$$\begin{aligned} &-\frac{\mathrm{Bi}^2 K h_t}{[1+\mathrm{Bi}(h+K)]^2} I_1 + \frac{\alpha_t I_2(\mathrm{Bi}h+1)}{\sin(\lambda)} \\ &+\alpha(\mathrm{Bi}h+1)\frac{\mathrm{d}\lambda}{\mathrm{d}h}h_t\left(\frac{I_3}{\sin(\lambda)} - \frac{\cos\lambda}{\sin^2\lambda} I_2\right) + \frac{\alpha \mathrm{Bi} h_t I_2}{\sin\lambda} = -\frac{\alpha\lambda^2 I_2}{A\sin(\lambda)}. \end{aligned} \tag{A1}$$

Solving for α_t:

$$\alpha_t = -\frac{\sin(\lambda)}{\mathrm{Bi}h+1}\frac{\mathrm{Bi}^2 K h_t}{[1+\mathrm{Bi}(h+K)]^2}\frac{I_1}{I_2} - \alpha h_t\left(\frac{\mathrm{d}\lambda}{\mathrm{d}h}\frac{I_3}{I_2} - \frac{\mathrm{d}\lambda}{\mathrm{d}h}\cot\lambda + \frac{\mathrm{Bi}}{\mathrm{Bi}h+1}\right) - \frac{\alpha\lambda^2}{A}, \tag{A2}$$

where the integrals are (using (22) to simplify)

$$I_1 = \int_{-1}^{0}(y+1)\sin\lambda(y+1)\,\mathrm{d}y = -\frac{\cos(\lambda)\lambda - \sin(\lambda)}{\lambda^2} = -\frac{[1+\mathrm{Bi}(h+K)]\cos(\lambda)}{\lambda \mathrm{Bi} K}, \tag{A3}$$

$$I_2 = \int_{-1}^{0}\sin^2(\lambda(y+1))\,\mathrm{d}y = \frac{\lambda - \cos(\lambda)\sin(\lambda)}{2\lambda} = \frac{\mathrm{Bi}K + (\mathrm{Bi}h+1)\cos^2(\lambda)}{2\mathrm{Bi}K}, \tag{A4}$$

$$\begin{aligned} I_3 &= \int_{-1}^{0}(y+1)\cos(\lambda(y+1))\sin(\lambda(y+1))\,\mathrm{d}y \\ &= \frac{1}{4\lambda^2}\left[\lambda + \cos(\lambda)\sin(\lambda) - 2\lambda\cos^2(\lambda)\right] = \frac{\mathrm{Bi}K - (1+\mathrm{Bi}h+2\mathrm{Bi}K)\cos^2(\lambda)}{4\lambda\mathrm{Bi}K}, \end{aligned} \tag{A5}$$

and from (22),

$$\frac{\mathrm{d}\lambda}{\mathrm{d}h} = \frac{-\mathrm{Bi}\lambda}{\mathrm{Bi}h + 1 + \mathrm{Bi}K\sec^2(\lambda)}.$$

The equation derived is then of the form (26a) with the given expressions for coefficients $C_j(h)$, $j = 1, 2, 3$.

Appendix B: Long- and short-wave instability criteria in terms of angle and typical film thickness

In an experiment, it is easiest to control the angle θ, as well as the height h_0 through the inlet flux. It is therefore useful to separate out the dependencies of each non-dimensional group on these parameters, and rewrite the long-wave

criticality condition (15b). We follow the approach used in [9], and write

$$\mathrm{Re} = \frac{\chi}{2}\sin\theta, \qquad \mathrm{Ma} = \frac{M}{\chi^{2/3}\sin\theta}, \qquad \mathrm{Bi} = B\chi^{1/3}, \qquad \mathrm{We} = \frac{\mathrm{Ka}}{\chi^{2/3}\sin\theta}, \tag{B1}$$

where

$$\chi = \frac{gh_0^3}{\nu^2}, \qquad M = \frac{\gamma(T_b - T_a)}{\rho\nu^{4/3}g^{1/3}}, \qquad B = \frac{\beta\nu^{2/3}}{\kappa_l g^{1/3}}, \qquad \mathrm{Ka} = \frac{\sigma_0}{\rho\nu^{4/3}g^{1/3}}, \tag{B2}$$

are the reduced parameters. Here Ka is called the Kapitza number, and χ contains the dependence on h_0. Let $\theta = \theta_c$ when $\mathrm{Re} = \mathrm{Re}_0$, then (15b) becomes

$$\frac{\chi}{2}\sin\theta_c = \frac{5}{4}\frac{\cos\theta_c}{\sin\theta_c} - \frac{15}{8}\frac{MB}{\chi^{1/3}\sin\theta_c(1 + B\chi^{1/3} + B_w)^2}, \tag{B3}$$

where $B_w = \mathrm{Bi}K = \beta d/\kappa_s$. In an experimental set-up, one could impose a given inlet thickness (so that χ is constant) or a given inlet flux, given by $q_0 = h_0^3 g\sin\theta/(3\nu) = (\nu/3)\chi\sin\theta$, in which case χ is proportional to $(\sin\theta)^{-1}$. In the first case, we obtain a quadratic in $\sin^2\theta_c$ and may solve to find

$$\sin^2\theta_c = \frac{5}{8\chi^2}\sqrt{25 + 16\chi^2 + 60\chi\mathcal{B}} - \frac{25}{8\chi^2} - \frac{15}{4}\frac{\mathcal{B}}{\chi}, \tag{B4}$$

where $\mathcal{B} = MB/[\chi^{1/3}(1 + B\chi^{1/3} + B_w)^2]$. Note that for sufficiently large $\mathcal{B}$ this will have no real solution, as then the Marangoni effect destabilizes the flat film at any angle. In the second case, when a given inlet flux is imposed, Eq. (B3) results in a more complicated equation for the critical angle that can be solved numerically.

Next, we examine the critical non-dimensional parameter $\mathrm{We}/(A^2\mathrm{Ma})$ that appears in the criterion for the existence of the short-wave instability (34). First, we write

$$A = \mathcal{A}\chi^{1/3}\sin\theta, \tag{B5}$$

where

$$\mathcal{A} = \frac{d^2 g^{2/3}}{2\alpha_s\nu^{1/3}}. \tag{B6}$$

We now have

$$\frac{\mathrm{We}}{A^2\mathrm{Ma}} = \frac{\mathrm{Ka}}{\mathcal{A}^2 M}\frac{1}{\chi^{2/3}\sin^2\theta}.$$

The short-wave instability occurs when this non-dimensional group is sufficiently small. For a given fluid (so that Ka is fixed), this can be achieved by requiring that the liquid film is sufficiently thick (so that χ is large), and/or the substrate is sufficiently thick (so that $\mathcal{A}$ is large) and/or the temperature difference $T_b - T_a$ is sufficiently large (so that M is large). We would also need to require that the angle θ is not near-horizontal (so that $\sin\theta$ is not too small).

[1] P. L. Kapitza and S. P. Kapitza, "Wave flow of thin layers of a viscous fluid," Zh. Eksp. Teor. Fiz **19**, 105 (1949).
[2] J. M. Floryan, S. H. Davis, and R. E. Kelly, "Instabilities of a liquid film flowing down a slightly inclined plane," Phys. Fluids **30**, 983–989 (1987).
[3] D. A. Goussis and R. E. Kelly, "Surface-wave and thermocapillary instabilities in a liquid-film flow," J. Fluid Mech. **223**, 25–45 (1991).
[4] S. Kalliadasis, C. Ruyer-Quil, B. Scheid, and M. G. Velarde, *Falling Liquid Films*, Applied Mathematical Sciences, Vol. 176 (Springer Verlag London, London, 2012) p. 440.
[5] D. A. Goussis and R. E. Kelly, "On the thermocapillary instabilities in a liquid layer heated from below," Int. J. Heat Mass Transfer **33**, 2237–2245 (1990).
[6] J. R. A. Pearson, "On convection cells induced by surface tension," J. Fluid Mech. **4**, 489–500 (1958).
[7] M. C. Cross and P. C. Hohenberg, "Pattern-formation outside of equilibrium," Rev. Mod. Phys. **65**, 851–1112 (1993).
[8] S. Sreenivasan and S. P. Lin, "Surface tension driven instability of a liquid film flow down a heated incline," Int. J. Heat Mass Transfer **21**, 1517–1526 (1978).

[9] S. Kalliadasis, E. A. Demekhin, C. Ruyer-Quil, and M. G. Velarde, "Thermocapillary instability and wave formation on a film falling down a uniformly heated plane," J. Fluid Mech. **492**, 303–338 (2003).

[10] P. M. J. Trevelyan and S. Kalliadasis, "Wave dynamics on a thin-liquid film falling down a heated wall," J. Eng. Math. **50**, 177–208 (2004).

[11] C. Ruyer-Quil, B. Scheid, S. Kalliadasis, M. G. Velarde, and R. K. Zeytounian, "Thermocapillary long waves in a liquid film flow. Part 1. Low-dimensional formulation," J. Fluid Mech. **538**, 199–222 (2005).

[12] B. Scheid, C. Ruyer-Quil, S. Kalliadasis, M. G. Velarde, and R. K. Zeytounian, "Thermocapillary long waves in a liquid film flow. Part 2. Linear stability and nonlinear waves," J. Fluid Mech. **538**, 223–244 (2005).

[13] P. M. J. Trevelyan, B. Scheid, C. Ruyer-Quil, and S. Kalliadasis, "Heated falling films," J. Fluid Mech. **592**, 295–334 (2007).

[14] O. A. Kabov, B. Scheid, I. A. Sharina, and J. C. Legros, "Heat transfer and rivulet structures formation in a falling thin liquid film locally heated," Int. J. Therm. Sci. **41**, 664–672 (2002).

[15] S. Kalliadasis, A. Kiyashko, and E. A. Demekhin, "Marangoni instability of a thin liquid film heated from below by a local heat source," J. Fluid Mech. **475**, 377–408 (2003).

[16] J. M. Skotheim, U. Thiele, and B. Scheid, "On the instability of a falling film due to localized heating," J. Fluid Mech. **475**, 1–19 (2003).

[17] P. M. J. Trevelyan, S. Kalliadasis, J. H. Merkin, and S. K. Scott, "Dynamics of a vertically falling film in the presence of a first-order chemical reaction," Phys. Fluids **14**, 2402–2421 (2002).

[18] P. M. J. Trevelyan and S. Kalliadasis, "Dynamics of a reactive falling film at large Péclet numbers. I. Long-wave approximation," Phys. Fluids **16**, 3191–3208 (2004).

[19] P. M. J. Trevelyan and S. Kalliadasis, "Dynamics of a reactive falling film at large Péclet numbers. II. Nonlinear waves far from criticality: Integral-boundary-layer approximation," Phys. Fluids **16**, 3209–3226 (2004).

[20] C. M. Gramlich, Serafim Kalliadasis, G. M. Homsy, and C. Messer, "Optimal leveling of flow over one-dimensional topography by Marangoni stresses," Phys. Fluids **14**, 1841–1850 (2002).

[21] S. Saprykin, P. M. J. Trevelyan, R. J. Koopmans, and S. Kalliadasis, "Free-surface thin-film flows over uniformly heated topography," Phys. Rev. E **75**, 026306 (2007).

[22] D. J. Benney, "Long waves on liquid films," J. Math. Phys. **45**, 150–155 (1966).

[23] B. Gjevik, "Occurrence of finite-amplitude surface waves on falling liquid films," Phys. Fluids **13**, 1918–1925 (1970).

[24] C. Ruyer-Quil and P. Manneville, "Modeling film flows down inclined planes," Eur. Phys. J. B **6**, 277–292 (1998).

[25] A. Pumir, P. Manneville, and Y. Pomeau, "On solitary waves running down an inclined plane," J. Fluid Mech. **135**, 27–50 (1983).

[26] A. Oron and O. Gottlieb, "Nonlinear dynamics of temporally excited falling liquid films," Phys. Fluids **14**, 2622–2636 (2002).

[27] B. Scheid, C. Ruyer-Quil, U. Thiele, O. A. Kabov, J. C. Legros, and P. Colinet, "Validity domain of the Benney equation including the Marangoni effect for closed and open flows," J. Fluid Mech. **527**, 303–335 (2005).

[28] V. Ya Shkadov, "Wave flow regimes of a thin layer of viscous fluid subject to gravity," Fluid Dyn. **2**, 29–34 (1967).

[29] R. B. Bird, W. E. Stewart, and E. N. Lightfoot, *Transport Phenomena*, 3rd ed. (Wiley, 2007).

[30] H. Schlichting and K. Gersten, *Boundary-Layer Theory* (Springer Science & Business Media, 2000).

[31] C. Ruyer-Quil and P. Manneville, "Improved modeling of flows down inclined planes," Eur. Phys. J. B **15**, 357–369 (2000).

[32] C. Ruyer-Quil and P. Manneville, "Further accuracy and convergence results on the modeling of flows down inclined planes by weighted-residual approximations," Phys. Fluids **14**, 170–183 (2002).

[33] M. Pradas, D. Tseluiko, and S. Kalliadasis, "Rigorous coherent-structure theory for falling liquid films: Viscous dispersion effects on bound-state formation and self-organization," Phys. Fluids **23**, 044104 (2011).

[34] L. A. Dávalos-Orozco, "The effect of the thermal conductivity and thickness of the wall on the nonlinear instability of a thin film flowing down an incline," Int. J. Non Linear Mech. **47**, 1–7 (2012).

[35] L. A. Dávalos-Orozco, "Stability of thin liquid films falling down isothermal and nonisothermal walls," Interfac. Phenom. Heat Transfer **1**, 93–138 (2013).

[36] T. Gambaryan-Roisman, "Marangoni convection, evaporation and interface deformation in liquid films on heated substrates with non-uniform thermal conductivity," Int. J. Heat Mass Transfer **53**, 390–402 (2010).

[37] T. Gambaryan-Roisman, "Marangoni-induced deformation of evaporating liquid films on composite substrates," J. Eng. Math. **73**, 39–52 (2012).

[38] A. Alexeev, T. Gambaryan-Roisman, and P. Stephan, "Marangoni convection and heat transfer in thin liquid films on heated walls with topography: Experiments and numerical study," Phys. Fluids **17**, 062106 (2005).

[39] W. D. Ristenpart, P. G. Kim, C. Domingues, J. Wan, and H. A. Stone, "Influence of substrate conductivity on circulation reversal in evaporating drops," Phys. Rev. Lett. **99**, 234502 (2007).

[40] E. J. Doedel, R. Champneys, F. Dercole, T. F. Fairgrieve, Yu. A. Kuznetsov, B. Oldeman, R. C. Paffenroth, B. Sandstede, X. J. Wang, and C. H. Zhang, "Auto-07p," Montreal Concordia University (2007), http://indy.cs.concordia.ca/auto/ (last accessed 22/03/2016).

[41] S. Kalliadasis, J. Yang, and A. De Wit, "Fingering instabilities of exothermic reaction-diffusion fronts in porous media," Phys. Fluids **16**, 1395–1409 (2004).

[42] P. Gaspard, "Local birth of homoclinic chaos," Physica D **62**, 94–122 (1993).

[43] Y. A. Kuznetsov, *Elements of Applied Bifurcation Theory*, Vol. 112 (Springer Science & Business Media, 2013).

[44] P. Kent and J. Elgin, "Traveling-waves of the Kuramoto-Sivashinsky equation - period-multiplying bifurcations," Nonlinearity **5**, 899–919 (1992).

[45] P. Glendinning and C. Sparrow, "Local and global behavior near homoclinic orbits," J. Stat. Phys. **35**, 645–696 (1984).
[46] M. Pradas, S. Kalliadasis, and D. Tseluiko, "Binary interactions of solitary pulses in falling liquid films," IMA J. Appl. Math. **77**, 408–419 (2012).
[47] M. Pradas, D. Tseluiko, C. Ruyer-Quil, and S. Kalliadasis, "Pulse dynamics in a power-law falling film," J. Fluid Mech. **747**, 460–480 (2014).
[48] D. Tseluiko and S. Kalliadasis, "Weak interaction of solitary pulses in active dispersive-dissipative nonlinear media," IMA J. Appl. Math. **79**, 274–299 (2014).
[49] T. S. Lin, M. Pradas, S. Kalliadasis, D. T. Papageorgiou, and D. Tseluiko, "Coherent structures in nonlocal dispersive active-dissipative systems," SIAM J. Appl. Math. **75**, 538–563 (2015).
[50] E. A. Chinnov and O. A. Kabov, "Marangoni effect on wave structure in liquid films," Microgravity Sci. Tech. **19**, 18–22 (2007).
[51] M. Rietz, W. Rohlfs, R. Kneer, and B. Scheid, "Experimental investigation of thermal structures in regular three-dimensional falling films," Eur. Phys. J–Spec. Top. **224**, 355–368 (2015).
[52] R. Mathie and C.N. Markides, "Heat transfer augmentation in unsteady conjugate thermal systems. Part I: Semi-analytical 1-D framework," Int. J. Heat Mass Trans. **56**, 802–818 (2013).
[53] R. Mathie, H. Nakamura, and C. N. Markides, "Heat transfer augmentation in unsteady conjugate thermal systems. Part II: Applications," Int. J. Heat Mass Trans. **56**, 819–833 (2013).
[54] C. N. Markides, R. Mathie, and A. Charogiannis, "An experimental study of spatiotemporally resolved heat transfer in thin liquid-film flows falling over an inclined heated foil," Int. J. Heat Mass Trans. **93**, 872–888 (2016).
[55] F. Denner, M. Pradas, A. Charogiannis, C. N. Markides, B. G. M. van Wachem, and S. Kalliadasis, "Self-similarity of solitary waves on inertia-dominated falling liquid films," Phys. Rev. E **93**, 033121 (2016).
[56] F. Denner, A. Charogiannis, M. Pradas, C. N. Markides, B. G. M. van Wachem, and S. Kalliadasis, "Solitary waves on falling liquid films in the drag-inertia regime: computations and experiments," Submitted.
[57] D. Tseluiko and D. T. Papageorgiou, "A global attracting set for nonlocal Kuramoto-Sivashinsky equations arising in interfacial electrohydrodynamics," Eur. J. Appl. Math. **17**, 677–703 (2006).